A Review of Level-Set Modeling in Epitaxial Growth and Alloys Solidification

Frederic Gibou[a,b], Ron Fedkiw[c], Russel Caflisch[d], Stanley Osher[e]

[a]*Department of Mechanical Engineering, University of California, Santa Barbara, CA 93106*
[b]*Department of Computer Science, University of California, Santa Barbara, CA 93106*
[c]*Department of Computer Science, Stanford University, CA 94305*
[d]*Courant Institute of Mathematical Sciences, New York University, N.Y. 10012*
[e]*Department of Mathematics, University of California, Los Angeles, CA 90095*

Abstract

Level-set methods provide a powerful computational framework for simulating free boundary problems in materials science. This paper presents a unified perspective on their application to two distinct phenomena: multicomponent alloy solidification and epitaxial island growth. Although these problems differ significantly in physical mechanisms and characteristic length scales, they can both be effectively addressed within the level-set framework, highlighting the versatility of the method across diverse applications. We outline the mathematical formulations and highlight computational advances and common features across applications. This overview highlights the role of level-set methods as a foundational tool in predictive materials modeling.

Keywords: Level-Set, Computational Materials, Metal Additive Manufacturing, Solidification, Epitaxy

1. Introduction

The level-set method of Osher and Sethian [1] has emerged as a versatile computational framework for simulating interface dynamics. Its implicit representation of interfaces allows it to naturally handle topological changes and to impose sharp boundary conditions at the exact location of the interface with controlled accuracy. The level-set method has had tremendous success in diverse fields. In fluid dynamics, it has been widely employed to model a broad spectrum of multiphase flow phenomena. Representative applications include two-phase and free-surface flows [2, 3, 4, 5, 6, 7], Hele–Shaw flows and incompressible flows in complex geometries [8, 9], compressible detonation dynamics [10], droplet–surface interactions, and coupled problems involving fluid–solid or incompressible–compressible interfaces [11, 12, 13]. The level-set method has also made a significant impact in image processing. For instance, level-set–based feature-preserving techniques have been developed to smooth noisy surfaces, in a manner closely related to diffusion-based image processing methods [14]. Comprehensive overviews of these approaches can be found in the book and review articles on the subject [15, 16]. In computer graphics, the level-set method has been widely adopted to simulate complex fluid–structure interactions, including the two-way coupling between fluids and thin deformable solids such as cloth or rigid shells [17]. It has also been employed to generate highly realistic animations of water dynamics [18, 19, 20, 21], as well as to capture the visual complexity of phenomena such as flames [22] and bubbles [23]. The level-set method has also found extensive application in problems of optimization and shape reconstruction. Notable examples include its use in inverse problem techniques for the design of photonic crystals [24], the reconstruction of surfaces from point clouds [25], and the optimization of geometries under constraints [26]. It has further been employed to determine optimal shapes for structural design [27, 28] and to reconstruct solvent-excluded surfaces of large biomolecules [29, 30]. Beyond these applications, the level-set method has been applied to problems in self-assembly of diblock copolymers, including the solution of inverse problems that identify confinement geometries guiding block copolymer assembly toward

prescribed target patterns in lithography [31, 32, 33, 34, 35, 36]. A broader overview of level-set approaches for inverse problems and optimal design can be found in [37].

Hybrid strategies have also been investigated, where the level-set method is coupled with other interface-tracking techniques, such as volume-of-fluid (VOF) or particle-based methods, to enhance accuracy and mass conservation [38, 39, 40]. For comprehensive perspectives, the reader is referred to several key reviews and monographs on the subject [41, 42, 43, 44]. In the field of materials science, these developments have enabled the formulation of sophisticated models for processes governed by evolving free boundaries, thereby extending the versatility of the level-set method to a wide range of technologically relevant phenomena.

This paper presents a unified perspective on the application of level-set methods to two distinct, yet thematically linked, problems in materials science:

1. The modeling of solidification in multicomponent alloys in the context of additive manufacturing (AM) using a sharp-interface formulation.
2. The modeling of epitaxial growth using an island dynamics model (IDM).

These applications differ in scale and governing physics, yet benefit from the level-set method's strengths in capturing evolving interfaces. Level-set methods have been applied to many other applications in materials and we refer the interested reader to [45] and the references therein. Taken together, these applications demonstrate the breadth and robustness of level-set methods in modeling free boundary problems that differ significantly in physical mechanisms and characteristic length scales. This review brings together these perspectives and highlights the method's contribution to advancing predictive simulation capabilities in materials science.

1.1. Alloy Solidification

Additive manufacturing holds immense promise for the development of advanced engineering components, particularly through its unique ability to fabricate complex three-dimensional geometries that would be difficult or impossible to achieve using conventional manufacturing techniques. Beyond geometric flexibility, AM also enables site-specific control over material properties by tuning processing parameters and thermal histories at a localized scale [46, 47, 48, 49, 50, 51]. This capability opens new pathways for the design and optimization of performance-critical parts in aerospace, biomedical, and energy systems. Recent studies have demonstrated the potential of AM to tailor microstructure and phase distribution during fabrication, thereby enhancing strength, ductility, and fatigue resistance in targeted regions of a component [46, 47, 48, 49, 50, 51].

Realizing the full potential of AM requires a fundamental understanding of the complex, multiphysics phenomena (heat transfer, mass diffusion, and fluid flow) that occur during solidification and how they influence the resulting microstructures and properties. Key features such as solute segregation, grain morphology, crystallographic orientation distribution, and defect formation (e.g., pores and cracks) are governed by the conditions at the solid-liquid interface during the melt pool evolution. Among the most critical solidification parameters are the local interface velocity (R) and the thermal gradient (G), which can span several orders of magnitude within a single melt pool and vary spatially and temporally during processing.

Designing AM-processed materials with targeted microstructures and properties therefore demands predictive models that can map solidification regimes (planar, cellular, columnar, and equiaxed growth) onto the (G, R) space for specific alloy systems. Although several models exist to predict structural transitions, such as the columnar-to-equiaxed transition (CET) [52, 53], they often rely on empirical parameters that are difficult to measure or estimate experimentally and were originally developed under unidirectional growth conditions, which are not representative of AM melt pool environments. As a result, these models frequently lack predictive capability under the complex thermal conditions imposed by scanning strategies and beam parameters. There remains a significant knowledge gap linking thermal transport, fluid flow, solute redistribution, and microstructure evolution, especially in multicomponent alloy systems.

In response to this need, a wide range of numerical strategies have been developed to simulate solidification. These approaches generally fall into three categories: cellular automata (CA) methods [54], phase-field or other diffuse-interface methods [55, 56, 57, 58], and sharp-interface methods

[59, 60, 61, 62, 63, 64, 65]. CA methods are computationally efficient but are rule-based rather than physics-based, limiting their fidelity. Phase-field methods offer a rigorous continuum approach in which the solid-liquid interface is described by a diffuse transition zone. However, while phase-field theory is asymptotically convergent to sharp-interface descriptions in the limit of vanishing interface thickness, practical implementations require artificially broadened interfaces, which may reduce accuracy for highly localized phenomena. To the best of our knowledge, there is currently no phase-field approach that can consider more than ternary systems. Considering a diffuse interface has also been considered within the level-set method [58], using the level-set method to track the interface but solving transport equations using smeared boundary conditions. This approach has the advantage of being simple but only approximately satisfies boundary conditions such as the Gibbs-Thomson relation.

Sharp-interface methods, on the other hand, explicitly model the solid-liquid boundary as a discontinuity. While they require sophisticated algorithms for interface tracking and for enforcing boundary conditions, they offer the advantage of faithfully representing the true macroscale physical description. In the case of a pure substance, where only the temperature field is solved, the early application of the level-set method was introduced by [66], who employed a boundary integral formulation to compute the temperature. This was later followed by the work of [59], who solved the temperature equation directly on a grid. In [59], the boundary condition at the interface was implemented using the method of Mayo [67], resulting in a second-order accurate scheme but yielding a non-symmetric linear system. Subsequently, [68] proposed a symmetric discretization of the problem, which was later extended to a fourth-order accurate scheme (albeit again producing a non-symmetric system) in [69]. This line of work was further extended in [62] to adaptive grids, achieving second-order accuracy for both the temperature field and its gradient in the context of the diffusion equation, and resulting in a fully second-order accurate method for pure substances. The level-set methodology was later extended to binary systems in [65, 64].

Truly sharp-interface simulations have been largely limited to binary alloys, leaving a gap in modeling capabilities for more realistic multicomponent systems. This gap has recently been addressed in [70], where a sharp-interface computational framework for multicomponent alloy solidification was introduced. The model couples temperature evolution, solute diffusion, and interface motion, capturing the complex interplay of physical phenomena at the solid-liquid boundary. Key physical effects, including crystallographic anisotropy, capillarity, and solute rejection, are resolved discretely as macroscopic discontinuities, rather than through approximate smoothing. A distinctive feature of the model is its use of thermodynamically consistent, composition-dependent liquidus slopes and partition coefficients, obtained from the PANDAT$^{\text{TM}}$ database, allowing accurate representation of local equilibrium at the interface.

Numerically, the framework leverages adaptive mesh refinement on quadtree grids and is optimized for scalable performance on parallel computing architectures. This allows for physically realistic simulations under thermal conditions characteristic of AM, such as high cooling rates and steep temperature gradients. The approach has been demonstrated on the solidification of Co-Al-W alloys, a ternary system relevant to structural applications, and has considered simulation of a penta-alloy. To the best of our knowledge, this work represents the first sharp-interface computational engine capable of simulating solidification in alloys with an arbitrary number of alloying elements.

1.2. Epitaxial Growth

Epitaxial growth underlies the fabrication of many modern electronic and optoelectronic devices, ranging from transistors and quantum dot lasers to advanced memory architectures and catalysts, by enabling the controlled deposition of atoms and molecules onto heated substrates, where they assemble into crystalline layers with atomic-scale precision. The resulting structures exhibit extremely low defect densities, which are essential for optimal device performance. However, simulating this process is difficult because the relevant length and time scales span many orders of magnitude: from submonolayer atomic events to the evolution of surface morphology over lateral scales of several microns or more. A comprehensive theoretical framework must accurately describe atomistic phenomena such as surface diffusion, nucleation, and island coalescence, as well as the

transition to multilayer growth regimes, which can result in kinetic roughening. The morphology of the growing film is sensitive to experimentally tunable parameters such as the ratio of the surface diffusion constant D to the deposition flux F, which governs whether atoms integrate smoothly into existing islands or form new nucleation sites. Capturing these mechanisms in a model that is both quantitatively predictive and computationally feasible across multiple regimes is a significant challenge. Ideally, such a model should be applicable to a wide range of homoepitaxial and heteroepitaxial systems, compatible with various growth techniques, and capable of resolving dynamic processes from atomic to device scales.

Epitaxial growth underlies the fabrication of many modern electronic and optoelectronic devices, ranging from transistors and quantum dot lasers to advanced memory architectures and catalysts, by enabling the controlled deposition of atoms and molecules onto heated substrates, where they assemble into crystalline layers with atomic-scale precision [71, 72, 73, 74]. The resulting structures exhibit extremely low defect densities, which are essential for device performance. However, simulating this process is challenging because the involved length and time scales span many orders of magnitude, from submonolayer atomic events to surface morphology evolution across lateral scales of several microns or more. This disparity necessitates multiscale modeling frameworks that span atomistic, mesoscale, and continuum descriptions [75, 76]. A comprehensive theoretical framework must accurately describe atomistic phenomena such as surface diffusion, nucleation, and island coalescence, as well as the transition to multilayer growth regimes, which can result in kinetic roughening. The morphology of the growing film is sensitive to experimentally tunable parameters such as the ratio of the surface diffusion constant D to the deposition flux F, which governs whether atoms integrate smoothly into existing islands or form new nucleation sites. Capturing these mechanisms in a model that is both quantitatively predictive and computationally feasible across multiple regimes is a significant challenge [77, 78]. Ideally, such a model should be applicable to a wide range of homoepitaxial and heteroepitaxial systems, compatible with various growth techniques, and capable of resolving dynamic processes from atomic to device scales. Level-set simulations offer a powerful framework for studying these effects by bridging atomistic processes and continuum-scale behavior, making them particularly promising for the development of tools for engineering applications in advanced materials design.

Kinetic Monte Carlo (KMC) methods have long been a central tool for studying epitaxial growth, as they directly incorporate atomistic event rates derived from fundamental physical principles, thereby providing a natural framework for mimicking the underlying microscopic processes. Historically, one of the earliest applications of KMC to epitaxial growth was the work of [79], who developed a fast KMC algorithm for simulating molecular beam epitaxy. This contribution was instrumental in demonstrating that stochastic event-driven methods could efficiently capture deposition, diffusion, and nucleation processes central to epitaxial layer formation. Since then, KMC has become the standard approach for simulating epitaxial phenomena across a wide range of material systems. For example, [80] introduced a multiscale KMC algorithm specifically tailored for epitaxial growth, demonstrating how stochastic atomistic events can be systematically coupled with larger-scale morphological evolution. Earlier, [81] provided a comprehensive review of KMC simulations in the context of chemical vapor deposition, highlighting the versatility of the method in describing growth processes involving adsorption, diffusion, and reaction kinetics. In turn, [82] applied first-principles-based KMC simulations to heterogeneous catalysis, offering a paradigm for how physically rigorous event rates can yield predictive insights into complex surface processes. Recent advances highlight both the flexibility and the continuing relevance of KMC to contemporary materials science. For example, [83] applied large-scale KMC simulations to the epitaxial growth of graphene, providing insight into how growth kinetics and nucleation influence the morphology of two-dimensional materials. Their results underscore the ability of KMC to address the challenges of simulating extended time and length scales in emerging low-dimensional systems. Likewise, [84] used KMC to investigate the influence of growth conditions on the epitaxial growth of 3C–SiC(0001) vicinal surfaces. Their study illustrates the predictive power of KMC in technologically important heteroepitaxial systems, where temperature, flux, and miscut angle strongly affect step-flow dynamics and surface morphology.

Collectively, these studies illustrate how KMC serves as a bridge between fundamental atomic-

scale mechanisms and experimentally observable growth behavior. At the same time, despite their accuracy and physical fidelity, KMC simulations are computationally demanding, particularly when long-range interactions or extended spatiotemporal scales must be resolved, posing challenges for their application to larger systems or technologically relevant growth regimes. By contrast, level-set simulations provide a continuum-based alternative that efficiently bridges atomistic mechanisms with mesoscale and continuum-scale behavior. The level-set formulation enables a continuous representation of island boundaries, even as these coalesce, shrink, or evolve anisotropically. The Island Dynamics Model [85, 86, 87], developed in this framework, offers a continuum alternative to kinetic Monte Carlo simulations, efficiently capturing stochastic nucleation and interface motion via deterministic adatom flux at the islands' boundaries. A key advantage of the IDM and its level-set formulation is its significantly lower computational cost compared to Monte Carlo simulations when accounting for long-range interactions such as elastic forces arising from lattice mismatch.

1.3. Outline

Section 2 provides an overview of the level-set method, the core numerical algorithms on which it is based, and how boundary conditions are imposed in this implicit approach. Sections 3 and 4 present applications of the method to multicomponent alloy solidification and epitaxial growth, respectively. Finally, Section 5 offers concluding remarks and discusses future research directions.

2. The Level-Set Method

The level-set method, introduced by Osher and Sethian [1], represents a moving interface as the zero level set of a higher-dimensional scalar function. The interface evolves implicitly under a velocity field determined by the governing physical laws, allowing for natural handling of topological changes such as merging and pinching. The level-set function $\phi(\mathbf{x})$ is set to be negative in one phase (e.g. the liquid phase in a solidification process) that occupies the region denoted Ω^- and positive in the other phase (e.g. the solid phase in a solidification process) that occupies the region denoted Ω^+:

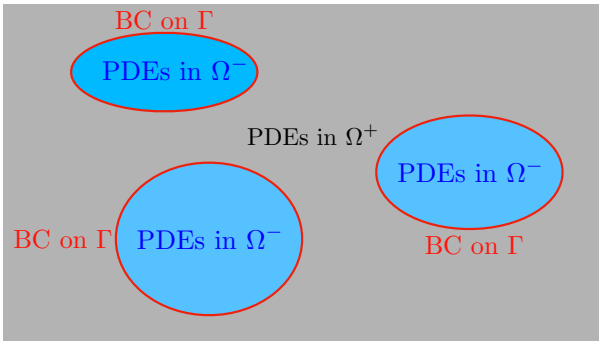

Figure 1: Typical level-set setup to free boundary problems.

$$\phi(\mathbf{x}) < 0, \forall \mathbf{x} \in \Omega^-, \quad \phi(\mathbf{x}) = 0, \forall \mathbf{x} \text{ on } \Gamma, \quad \phi(\mathbf{x}) > 0, \forall \mathbf{x} \in \Omega^+.$$

Figure 1 illustrates the level-set methodology for free-boundary problems. In this framework, the governing physical equations are solved in the regions Ω^- and Ω^+, while appropriate boundary conditions are prescribed on the evolving interface Γ. The procedure for imposing boundary conditions within the level-set framework is presented in Section 2.3, and the sets of partial differential equations governing each region are detailed in Section 3 for solidification and Section 4 for the IDM.

Although in principle the level function can be chosen to be any Lipschitz continuous function, a practical choice is to define the level-set function as the signed distance to the interface Γ. As the level-set function is deformed under its normal velocity, it is necessary to re-initialize it to a signed distance function. When the normal velocity exhibits strong anisotropy, it is necessary to perform the reinitialization procedure at every time step in order to maintain the signed-distance property. More generally, carrying out reinitialization at each step is a sound rule of thumb in scientific applications. A traditional approach is to solve the *reinitialization* equation [2]:

$$\phi_\tau + \text{sign}(\phi^0)(|\nabla\phi| - 1) = 0, \tag{1}$$

where τ is a pseudo-time step, taken in practice to correspond to a number of iterations between 10 and 15.

In materials science, this representation proves especially useful in problems where the interface dynamics depend on coupled processes such as diffusion, reaction kinetics, phase transformations, or mechanical deformation. The method's ability to maintain a sharp interface and its compatibility with structured or adaptive grids make it particularly well-suited for high-resolution simulations. In addition, the level-set representation provides a straightforward way to compute the normal vector, $\boldsymbol{n}$, to the boundary and its mean curvature, κ:

$$\boldsymbol{n} = \frac{\nabla\phi}{|\nabla\phi|}, \qquad \kappa = \nabla\cdot\boldsymbol{n} = \nabla\cdot\frac{\nabla\phi}{|\nabla\phi|}.$$

Given the normal velocity of the interface, $v_{\boldsymbol{n}} = \boldsymbol{v}\cdot\boldsymbol{n}$, derived from physical models, the level-set function is evolved under using the level-set equation:

$$\frac{\partial\phi}{\partial t} + v_{\boldsymbol{n}}|\nabla\phi| = 0. \tag{2}$$

2.1. Discretization of the Level-Set Equations

2.1.1. Spatial Discretization

The discretization of the normal and curvature are straightforward and are based on simple central differencing. The discretizations of the reinitialization equation (1) and the level-set equation (2) are more involved and are based on numerical advances on Hamilton-Jacobi solvers, themselves based on advances in computational methods for conservation laws. Since those equations can be solved in a dimension-by-dimension approach, it is enough to present the approach in one spatial dimension.

The Hamilton-Jacobi equation in one spatial dimension is written as:

$$\phi_t + H(\phi_x, x, t) = 0, \tag{3}$$

and its discretization takes the form:

$$\phi_i^{n+1} = \phi_i^n - \Delta t H_i^n(\phi_x^-, \phi_x^+),$$

where ϕ_x^-, ϕ_x^+ are the approximation of the left and right derivative of the level-set function ϕ^n and H_i^n is an approximation of the Hamiltonian H.

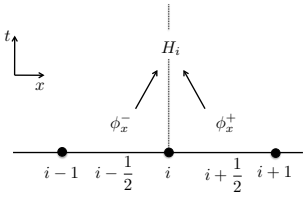

Figure 2: Framework for defining the numerical Hamiltonian H_i^n.

The first difficulty when considering numerically approximating the level-set equations is the fact that equations are nonlinear and therefore can produce shock and rarefaction solutions that require approximating derivatives of functions with steep gradients or kinks. Issued from progress made in the context of conservation laws, the schemes used are of the type ENO/WENO [88, 89, 90, 91]. The main idea behind those approaches is to create a customized stencil at each grid point in order to approximate derivatives, with the driving principle being to start from the standard upwind direction and add grid points to the stencil in such a way as to avoid regions of sharp gradients; sharp gradients can conveniently be estimated by creating a finite difference table at each grid points. The ENO/WENO schemes used in these studies are detailed in Appendix A.

Remarks:

1. We note that the use of ENO/WENO schemes, compared to a first-order upwind discretization, inevitably increases the computational cost by a factor of three to four, depending on the sophistication of the implementation. However, such high-order schemes are essential to mitigate the excessive numerical diffusion associated with simple upwinding, which would otherwise compromise the accuracy of the solution to the point of rendering the results unreliable.

2. In the case of uniform grids, the WENO scheme is typically used. In the case of adaptive grids, given the computational cost of accessing grid points that are not immediately in the neighborhood of a grid point at which we are seeking an approximation of the derivatives, we are limiting the ENO procedure to second-order accuracy in conjunction with the treatment of T-junction nodes described in section 2.2.

The second difficulty is to properly approximate, at each grid point, the Hamiltonian H_i^n depending on the values of ϕ_x^-, ϕ_x^+ (see Figure 2). This approximation must take into account nonlinear effects related to shocks and rarefaction waves, following the Godunov strategy that defines the Hamiltonian as follows:

$$H_i^n \approx \begin{cases} \min\limits_{\phi_x \in [\phi_x^-, \phi_x^+]} H(\phi_x), & \text{if } \phi_x^- \leq \phi_x^+, \\ \max\limits_{\phi_x \in [\phi_x^+, \phi_x^-]} H(\phi_x), & \text{if } \phi_x^- \geq \phi_x^+. \end{cases} \tag{4}$$

For example, in the case of the level-set equation (2), which can be re-written as follows to give a direct handle on the characteristic directions:

$$\phi_t + \frac{v_n \phi_x}{\sqrt{\phi_x^2 + \phi_y^2 + \phi_z^2}} \phi_x + \frac{v_n \phi_y}{\sqrt{\phi_x^2 + \phi_y^2 + \phi_z^2}} \phi_y + \frac{v_n \phi_z}{\sqrt{\phi_x^2 + \phi_y^2 + \phi_z^2}} \phi_z = 0,$$

the Godunov formula, gives the following discretization for the term ϕ_x term:

1. If $v_n \phi_x^- \leq 0$ and $v_n \phi_x^+ \leq 0$ discretize ϕ_x by ϕ_x^+.
2. If $v_n \phi_x^- \geq 0$ and $v_n \phi_x^+ \geq 0$ discretize ϕ_x by ϕ_x^-.
3. If $v_n \phi_x^- \leq 0$ and $v_n \phi_x^+ \geq 0$ set $\phi_x = 0$.
4. If $v_n \phi_x^- \geq 0$ and $v_n \phi_x^+ \leq 0$
   (a) If $|v_n \phi_x^+| \geq |v_n \phi_x^-|$ discretize ϕ_x by ϕ_x^+.
   (b) If $|v_n \phi_x^+| \leq |v_n \phi_x^-|$ discretize ϕ_x by ϕ_x^-.

The terms ϕ_y and ϕ_z are discretized similarly, the results are plugged into equation (2). The reinitialization equation is discretized almost identically by writing equation (1) as:

$$\phi_\tau + \text{sign}(\phi^0) \left(\frac{\phi_x}{\sqrt{\phi_x^2 + \phi_y^2 + \phi_z^2}} \phi_x + \frac{\phi_y}{\sqrt{\phi_x^2 + \phi_y^2 + \phi_z^2}} \phi_y + \frac{\phi_z}{\sqrt{\phi_x^2 + \phi_y^2 + \phi_z^2}} \phi_z - 1 \right) = 0.$$

2.1.2. TVD-RK3

The spatial discretization is traditionally coupled with a TVD-RK3 algorithm for the time evolution [88]. TVD stands for Total Variation Diminishing and can be written as a set of simple Euler steps in combination with linear averaging of the solution at intermediate steps. In the case of the Hamilton-Jacobi equation (3), we start from ϕ^n, and perform one Euler step to find a temporary $\tilde{\phi}^{n+1}$ at each grid point:

$$\frac{\tilde{\phi}_i^{n+1} - \phi_i^n}{\Delta t} + H_i^n = 0,$$

followed by another Euler step to find a temporary $\tilde{\phi}_i^{n+2}$:

$$\frac{\tilde{\phi}_i^{n+2} - \tilde{\phi}_i^{n+1}}{\Delta t} + H_i^{n+1} = 0,$$

where H_i^{n+1} is computed using equation (4) with ϕ_x^-, ϕ_x^+ computed from $\tilde{\phi}^{n+1}$. Once $\tilde{\phi}^{n+2}$ is found, we apply a weighted averaging procedure to find a temporary $\tilde{\phi}^{n+\frac{1}{2}}$:

$$\tilde{\phi}_i^{n+\frac{1}{2}} = \frac{3}{4}\phi_i^n + \frac{1}{4}\tilde{\phi}^{n+2}.$$

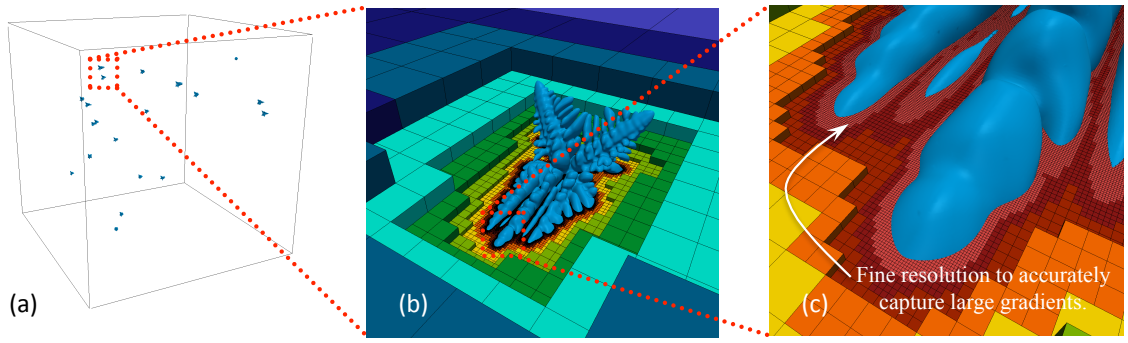

Figure 4: Simulation of crystal growth in 3D (a) with a zoom on one crystal (b) and a further zoom on the resolved thermal boundary layer (c). Figure adapted from [106].

Last, another Euler step is used to find a temporary $\tilde{\phi}_i^{n+\frac{3}{2}}$:

$$\frac{\tilde{\phi}_i^{n+\frac{3}{2}} - \tilde{\phi}_i^{n+\frac{1}{2}}}{\Delta t} + H_i^{n+\frac{1}{2}} = 0,$$

where $H_i^{n+\frac{1}{2}}$ is computed using equation (4) with ϕ_x^-, ϕ_x^+ computed from $\tilde{\phi}^{n+\frac{1}{2}}$. The updated solution ϕ^{n+1} at each grid point is defined by a weighted average: ϕ^{n+1}:

$$\phi_i^{n+1} = \frac{1}{3}\phi_i^n + \frac{2}{3}\tilde{\phi}_i^{n+\frac{3}{2}}.$$

We also refer the interested reader to other methodologies to reinitialize the level-set function that are not based on PDE evolution equations, such as the Fast Marching Method [92, 42, 93], the Fast Sweeping Method [94, 95] and their parallel versions [96, 97, 98], or other explicit approaches [99, 100, 101, 102, 103], as well as the recent work by Osher seeking to overcome the curse of dimensionality [104, 105] for Hamilton-Jacobi equations.

2.2. Adaptive Grid Refinement

The level-set method is known to exhibit a form of numerical error commonly referred to as "mass loss," wherein the evolving interface deviates slightly from the expected physical trajectory. This artifact, however, diminishes with grid refinement and results in a negligible loss of mass when sufficiently fine grids are used. Because the computational cost scales with the number of grid points and high resolution is primarily needed in the vicinity of the interface, adaptive mesh refinement (AMR) presents a particularly effective strategy. In addition, many problems in materials science are either diffusion-dominated or governed by partial differential equations with parabolic or elliptic components. These equations typically yield smooth solutions, except near interfaces where discontinuities or sharp gradients may arise. This further supports the use of adaptive grids, which concentrate computational resources where they are most needed while minimizing overall cost. An example of a three-dimensional crystal growth simulation is presented in Figure 4.

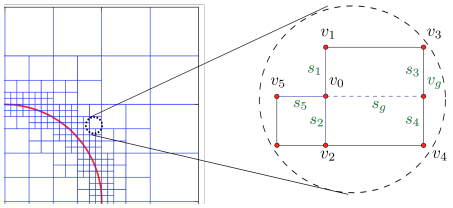

Figure 3: Zoom on a T-junction grid point.

In the context of AMR, quadtree and octree data structures representation of adaptive Cartesian grids offer optimal efficiency in terms of both memory usage and CPU cost. In [107], the authors proposed a straightforward discretization strategy applicable to level-set methods [108], parabolic and elliptic equations in irregular domains [62, 61, 109, 110, 111, 112, 113, 114, 115, 116], as well as the Navier-Stokes equations [117]. The core contribution lies in the treatment of T-junction grid

points, which are points on the grid where one (in 2D) or two (in 3D) neighboring grid points are missing, as illustrated in Figure 3. The authors introduced a definition for these missing neighbors that enables third-order accuracy:

$$u^G = \frac{s_4 u_3 + s_3 u_4}{s_3 + s_4} - \frac{s_3 s_4}{s_1 + s_2}\left(\frac{u_2 - u_0}{s_2} + \frac{u_1 - u_0}{s_1}\right).$$

This formulation allows the use of standard upwind or central differencing schemes as if the grid were uniform, while maintaining the desired level of accuracy. We note that given the computational cost of accessing grid points that are not immediately in the neighborhood of a grid point at which we are seeking an approximation of the derivatives, we are limiting the ENO procedure to second-order accuracy. We note that adaptive grids are particularly advantageous for elliptic and parabolic problems, i.e., those dominated by diffusion. In such cases, the solution is infinitely smooth away from the interface and can therefore be accurately resolved on relatively coarse grids. Near the interface, however, discontinuities in the solution and/or its flux require enhanced resolution, which can be efficiently provided by local grid refinement. For example, [118] demonstrated that an adaptive grid with a coarse 32×32 background resolution achieves the same level of accuracy as a uniform 256×256 grid, provided that the grid is locally refined to the effective 256×256 level within a narrow band around the interface. Building on the `p4est` library [119], which manages the distribution of adaptive grids across multiple processes, [106] developed the `casl` library, which implements level-set methods and standard solvers optimized for massively parallel architectures. Additional work utilizing the octree data structure includes that of [19, 21] and research on mainly compressible flows on AMR can be found in [120] and the references therein.

2.3. Imposing Boundary Conditions

An important advantage of the level-set method lies in its ability to impose sharp boundary conditions, namely, the capability to enforce conditions directly at the precise interface location with controlled accuracy (see sections 2.3.1, 2.3.2, and 2.3.3), while preserving the discontinuities in the solution and its flux. This capability is particularly important when modeling systems under the continuum assumption underpinning conservation laws, where rapid variations across physical interfaces are accurately represented as sharp discontinuities rather than smooth transitions. Boundary conditions typically fall into Dirichlet, Robin (with a sub case being Neumann) and jump conditions. In the context of solidification, the Gibbs-Tompson is a well-known Dirichlet physical boundary condition that describes the equilibrium temperature of the phase transition and the concentration of alloying elements have a jump across the solidification front. An example of Robin boundary condition will be discussed in the context of epitaxy (section **??**) that is responsible for mound formation.

The Ghost Fluid Method (GFM), originally introduced to capture sharp discontinuities in compressible flow and detonation problems [121, 122, 123, 124], has significantly influenced how sharp boundary conditions are imposed within the level-set framework. In the context of compressible flows, the central idea is to track the location of shocks and contact discontinuities using the level-set method, while maintaining two separate numerical solutions; one on each side of the interface representing the real fluid, and a ghost fluid that is defined as the real fluid plus the Rankine-Hugoniot jump condition. Thanks to the definition of a ghost fluid, the solution remains continuous across the interface and therefore avoids directly differentiating discontinuous functions, thereby eliminating the large numerical errors that would otherwise arise.

This simple yet powerful approach has been successfully extended to elliptic and parabolic problems. In particular, it has been applied to the Poisson and diffusion equations on irregular domains with Dirichlet boundary conditions, as well as to problems involving jump conditions. In this section, we briefly describe the methodology for jump, Dirichlet and Robin/Neumann conditions.

2.3.1. Jump Boundary Conditions

In the case of elliptic and parabolic equations, the jump conditions are given for the solution and its flux, i.e. of the form $[\mu \nabla u \cdot \boldsymbol{n}] = g$, where $g = g(\boldsymbol{x}, t)$ is a known function and μ is a variable coefficient (e.g. the thermal conductivity in a solidification problem). Figure 5 is an example of the imposing sharp jump conditions using the method of [125], illustrating that the jumps in the solution and its flux are indeed imposed at the discrete level. The first Ghost-Fluid approach replaced the jump in flux by its projection to each spatial dimension, resulting in a strategy that is simple since it allows a dimension-by-dimension approach to approximating the Laplace operator [126]. In the case where the tangential component of the jump in flux are crucial, this approach may introduce a numerical smearing of the tangential components that can pollute the solution. To address this limitation, three techniques have been proposed. The first, inspired by the work of [127], uses a Voronoi partition so that the degrees of freedom of the Voronoi cell are orthogonal to their edges, making the application of the approach of [126] accurate when tangential terms are important [128]. The second, known as xGFM [129], extends the Ghost Fluid Method by enforcing the full jump condition in the normal direction through an iterative process. The third approach, introduced in [125], constructs second-order accurate expressions for the solution on either side of the interface using normal derivatives of the solution. The difference between these expressions is then directly linked to the jump conditions in the solution and its flux. By approximating the local gradient via a least-squares fit using neighboring points, this method yields two candidate formulas for the ghost value. Interestingly, [125] observe that choosing the formula corresponding to the region with the smaller diffusion coefficient leads to a linear system with significantly improved conditioning. As illustrated in Figure 6, both the condition number and the numerical error in the solution and its gradient remain well-controlled (i.e. bounded), even in the presence of strong discontinuities in the diffusion coefficient. From a practical point of view, it is necessary to use the method in [125] to avoid smearing in the tangential component. We note, however, that for some applications such as incompressible flows without phase change nor Marangoni effects, tangential components are absent, and the approach of [126] can be employed instead, which is simpler to implement. In both cases, the resulting scheme achieves second-order accuracy in the maximum norm.

Figure 5: Example of a typical numerical solution of the Poisson equation with jump conditions on irregular domains.

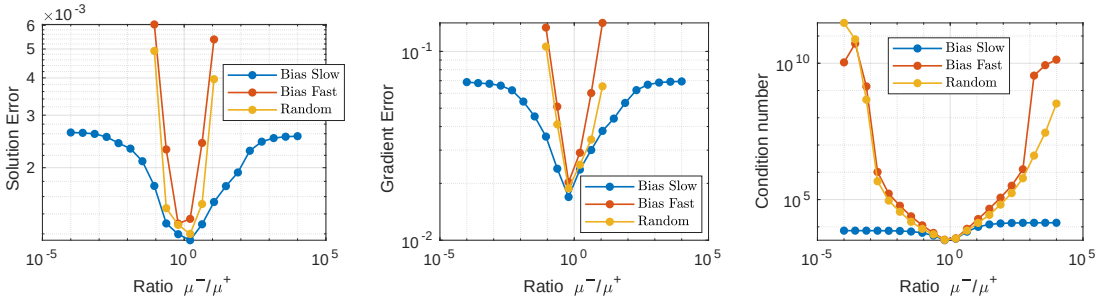

Figure 6: `conditioning test` in two spatial dimensions (each data point represents the maximum value among $10 \times 10 = 100$ different relative placements of an immersed interface on the computational grid). Figure adapted from [125].

2.3.2. Dirichlet Boundary Conditions

Solving elliptic or parabolic problems requires implicit discretizations, where a linear system of equations is built. Specifically, each line of the linear system is filled with the coefficients of the standard central differencing formula in each spatial direction. In cases where a specific value must be imposed on an irregular domain, the typical configuration is illustrated in Figure 7, where the solution exhibits a discontinuity in the deriva-

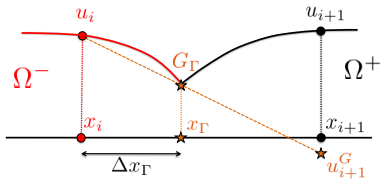

Figure 7: Definition of the ghost value u^G_{i+1} using a linear extrapolation. First, construct a linear interpolant $I(x) = ax + b$ of u such that $I(0) = u_i$ and $I(\Delta x_\Gamma) = u_\Gamma$. Then define $u^G_{i+1} = I(\Delta x)$. (Color online).

tive at the interface[1]. The ghost fluid method addresses this by defining a ghost value that still enables the use of standard central differencing while preserving the sharp interface behavior. This ghost value is defined by considering the extrapolation of the solution from one side of the interface to the other, which in turn gives the modified coefficients of the linear system for grid points adjacent to the interface. The order of accuracy and the symmetry of the linear system is detailed in [68, 69] and [130] summarizes which extrapolation to use depending on the problem considered.

2.3.3. Robin Boundary Conditions

Robin boundary conditions are commonly employed to model physical phenomena such as convective heat or mass exchange at boundaries, semi-permeable membranes, imperfect insulation, or radiative transfer, among many. In its most general form, Robin boundary conditions are written as $\dfrac{\partial u}{\partial \boldsymbol{n}} + \alpha\, u = g$, where $\alpha = \alpha(\boldsymbol{x}, t)$ and $g = g(\boldsymbol{x}, t)$ are given functions; in the case where $\alpha = 0$ the boundary condition is of Neumann type. Robin boundary conditions are important as they give a condition for the flux of the solution across the free boundary. An example of such application is given in section 4 for the simulation of mounding in epitaxial growth.

Although finite difference approaches extending the Ghost-Fluid Method for Dirichlet conditions of [68, 69], have been adapted to impose Robin boundary conditions within the level-set framework [131, 132, 133, 134, 135, 136], a finite volume approach is generally preferred due to its more natural incorporation of boundary fluxes and compatibility with conservative formulations. Through the use of the divergence theorem over each cell containing the zero-level set (see Figure 8), the boundary condition is naturally incorporated into the formulation, reducing the problem to computing fluxes across the boundary of the computational cell and the integration of a known function over the zero-level of the level-set function. Specifically, the discretization of the Laplace operator over a computational cell $C_{i,j}$, covered by the irregular domain Ω, is treated as follows:

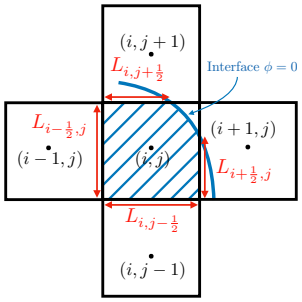

Figure 8: Local grid arrangement of a computational cell centered at (i, j) cut by an interface defined by the level-set function ϕ.

$$
\begin{aligned}
-\Delta u = f \quad &\Longleftrightarrow \quad -\int_{C_{i,j}\cap\Omega} \Delta u \, dC = \int_{C_{i,j}\cap\Omega} f \, dC \\
&\Longleftrightarrow \quad -\int_{\partial C_{i,j}\cap\Gamma} \nabla u \cdot \boldsymbol{n} \, dC = \int_{C_{i,j}\cap\Omega} f \, dC.
\end{aligned}
$$

The right-hand side of the last equality is approximated as $f_{i,j} \times \text{Area}(C_{i,j} \cap \Omega)$, whereas the left-hand side of the last equality can be approximated as:

$$
\begin{aligned}
- \quad & L_{i+\frac{1}{2},j} \frac{u_{i+1,j} - u_i, j}{\Delta x} - L_{i-\frac{1}{2},j} \frac{u_{i,j} - u_{i-1,j}}{\Delta x} \\
- \quad & L_{i,j+\frac{1}{2}} \frac{u_{i,j+1} - u_{i,j}}{\Delta x} - L_{i,j-\frac{1}{2}} \frac{u_{i,j} - u_{i,j-1}}{\Delta x} - \int_\Gamma (g - \alpha u) \, d\Gamma,
\end{aligned}
$$

where the $L_{i\pm\frac{1}{2},j\pm\frac{1}{2}}$ represent the length of the portion of the cell faces covered by the irregular domain (see Figure 8). Imposing Robin boundary conditions therefore boils down to approximating the integral of $(g - \alpha u)$ over an interface represented by the level-set function.

The first finite volume formulation of Robin boundary conditions within the level-set framework was introduced in [137], where the numerical integration of $(g - \alpha u)$ was based on the geometric

[1] In the case where, in addition, the solution itself is discontinuous, the numerical treatment outlined in section 2.3.2 is identical as it fully decouples the numerical solution on both sides of the interface.

approach developed in [113, 138, 139]. This method is second-order accurate in the maximum norm. We are not aware of alternative approaches for imposing Robin boundary conditions that achieve a comparable balance of simplicity and accuracy for interfaces that do not develop kinks. This methodology was subsequently extended to support adaptive grids and moving interfaces in [61]. While this approach produces symmetric linear systems that are desirable for their fast inversion using standard linear algebra numerical methods, the solution gradient is only first-order accurate. In turn, this limits free boundary problems to first-order accuracy if they depend on the solution gradient; typical examples in materials are those considered here. To solve that problem, [140] extended the work of [137] to produce second-order accurate solutions, albeit non-symmetric linear systems, where one of the main ingredients is the evaluation of the fluxes between cells that are discretized using the ideas of [141]. The methodology was then extended in [142] to the case where the boundary is piece-wise continuous, i.e., applicable to the case where the interface itself has kinks. The method retains second-order accuracy in the maximum norm, including on adaptive grids and in the presence of kinked interfaces, and thus constitutes the most advanced available approach.

3. Application - Solidification of Multicomponent Alloys in Additive Manufacturing

3.1. Sharp Interface Model

Consider the solidification of an alloy system composed of N+1 chemical species: a dominant solvent element that forms the primary matrix of the alloy, and N additional solute elements present in lesser concentrations. Such multicomponent alloy systems are representative of many technologically important materials, including high-entropy alloys and advanced superalloys, where the interactions between multiple solute elements and the solvent play a critical role in determining microstructural evolution during solidification. The thermodynamic and kinetic complexities introduced by the presence of multiple solutes (including solute partitioning, cross-diffusion effects, and non-linear phase equilibria) make the modeling and control of solidification processes in these systems particularly challenging. Accurate description of these phenomena is essential for predicting phase selection, morphology development, and segregation patterns, which ultimately govern the mechanical and functional properties of the solidified material.

We denote the evolving solid-liquid interface by $\Gamma(t)$, and define the domains within the computational domain Ω that are occupied by the solid and liquid phases as Ω^s and Ω^l. We also define the temperature, at time t and location $\boldsymbol{x}$, as $T = T(t, \boldsymbol{x})$ and the N different compositions as $C^J = C^J(t, \boldsymbol{x})$, $J \in [1, N]$ in the solid and liquid regions as:

$$T(t,\boldsymbol{x}) = \begin{cases} T^l(t,\boldsymbol{x}), & \boldsymbol{x} \in \Omega^l(t) \\ T^s(t,\boldsymbol{x}), & \boldsymbol{x} \in \Omega^s(t) \end{cases}, \quad \text{and} \quad C^J(t,\boldsymbol{x}) = \begin{cases} C^l_J(t,\boldsymbol{x}), & \boldsymbol{x} \in \Omega^l(t) \\ C^s_J(t,\boldsymbol{x}), & \boldsymbol{x} \in \Omega^s(t) \end{cases}, \quad J \in [1, N]\,.$$

In the absence of convective transport, the evolution of thermal and solutal fields is governed by diffusion-dominated processes. The energy and species conservation laws reduce to classical diffusion equations within each phase:

$$\rho^\nu {c_p}^\nu \partial_t T^\nu - \lambda^\nu \nabla^2 T^\nu = 0, \quad \boldsymbol{x} \in \Omega^\nu(t), \quad \nu = s, l, \tag{5}$$

$$\partial_t C^\nu_J - D^\nu_J \nabla^2 C^\nu_J = 0, \quad \boldsymbol{x} \in \Omega^\nu(t), \quad \nu = s, l, \quad J \in [1, N]\,, \tag{6}$$

where, ρ^ν, ${c_p}^\nu$, and λ^ν denote the mass density, specific heat capacity, and thermal conductivity, respectively, within each phase $\nu \in s, l$, corresponding to solid and liquid states. Similarly, D^ν_J represents the diffusivity of the J^{th} solute species in phase ν. The domains $\Omega^s(t)$ and $\Omega^l(t)$ evolve over time due to phase transformation at the solid-liquid interface.

For the sake of clarity and tractability, we assume constant material properties within each phase, i.e. ρ^ν, ${c_p}^\nu$, λ^ν, and D^ν_J are considered independent of temperature and composition. Although more sophisticated models may account for their dependence on local thermodynamic conditions, this simplification is often adequate for capturing the essential features of diffusion-driven solidification dynamics, and the resulting equations provide the foundation for more advanced models

incorporating interface kinetics, interfacial energy effects, and thermodynamic equilibrium conditions at the moving boundary. It is also important to note that in the context of multicomponent alloy solidification, it is standard practice to solve the energy conservation equation in both the liquid and solid phases, as thermal diffusion occurs at comparable timescales in both regions. In contrast, the governing diffusion equations for the chemical species are generally restricted to the liquid phase, a modeling choice that is justified by the fact that solute diffusion in the solid is several orders of magnitude slower than in the liquid and can, to a good approximation, be neglected over the solidification timescale. Consequently, the solid is often treated as a stationary phase with respect to solute transport, which simplifies the computational model without compromising accuracy. This assumption is widely adopted in the literature and forms the basis of many sharp-interface and phase-field models of alloy solidification.

In the modeling of multicomponent alloy solidification, the temperature and concentration fields must satisfy a series of thermodynamic and interfacial conditions at the evolving solid-liquid interface. A fundamental assumption in this framework is that the phase transformation occurs at local thermodynamic equilibrium. Consequently, the temperature field is continuous across the solidification front, leading to the condition:

$$[T] = 0, \quad \text{on } \Gamma(t), \tag{7}$$

where the jump operator $[\cdot]$ represents the difference in a field variable across the interface (i.e., $[T] = T^s - T^l$, with T^s and T^l denoting the temperatures on the solid and liquid sides, respectively). Furthermore, the temperature at the interface must satisfy a generalized Gibbs-Thomson condition that accounts for both interface kinetics and curvature effects:

$$T^l = T^{\text{liq}}\left(C_1, \ldots, C_N\right) + \epsilon_v(\boldsymbol{n}) v_{\boldsymbol{n}} + \epsilon_c(\boldsymbol{n})\kappa, \quad \text{on } \Gamma(t), \tag{8}$$

where $T^{\text{liq}}\left(C_1, \ldots, C_N\right)$ defines the local liquidus temperature as a function of the solute concentrations. The normal velocity of the interface is denoted $v_{\boldsymbol{n}}$, and κ represents the mean curvature of the interface, while $\epsilon_v(\boldsymbol{n})$ and $\epsilon_c(\boldsymbol{n})$ are the kinetic and capillary coefficients, respectively, which may depend on the orientation of the interface normal $\boldsymbol{n}$.

In classical solidification models, the liquidus temperature is often approximated as a linear function of composition:

$$T^{\text{liq}}\left(C_1, \ldots, C_N\right) = T_m + m_1 C_1 + \ldots + m_N C_N,$$

where T_m is the melting temperature of the pure solvent, and m_J are referred to as the liquidus slopes for the solutes $C_1, \ldots, C_N$. However, such linear approximations are insufficient for capturing the thermodynamic complexity of multicomponent alloys, where interactions between solutes can lead to highly nonlinear behavior in the phase diagram. To address this, [70] adopted a more general approach by allowing the liquidus temperature T^{liq} to be an arbitrary, composition-dependent, function. Accordingly, the liquidus slopes $m_J = \partial T^{\text{liq}} / \partial C_J$ are treated as functions of the local composition, enabling a more accurate and physically realistic description of the solidification process. For the numerical simulations reported in [70], the necessary thermodynamic data are obtained from the PANDAT™ database, which provides reliable multicomponent phase equilibria for engineering alloys (see Figure 9).

The thermal and chemical conditions at the solid-liquid interface play a critical role in determining the morphology and composition of the resulting microstructure. The thermal balance at the moving interface is governed by a Stefan-type condition, which enforces the conservation of energy by equating the net heat flux across the interface to the latent heat released or absorbed during the phase transition:

$$[\lambda \partial_{\boldsymbol{n}} T] = v_{\boldsymbol{n}} L_f, \quad \boldsymbol{x} \in \Gamma(t), \tag{9}$$

where L_f denotes the latent heat of fusion per unit volume, λ is the thermal conductivity, $\partial_{\boldsymbol{n}} T$ is the temperature gradient normal to the interface, and $v_{\boldsymbol{n}}$ is the normal velocity of the interface. This condition ensures that the local thermal field responds dynamically to the evolving interface and accommodates the release or absorption of latent heat associated with phase change.

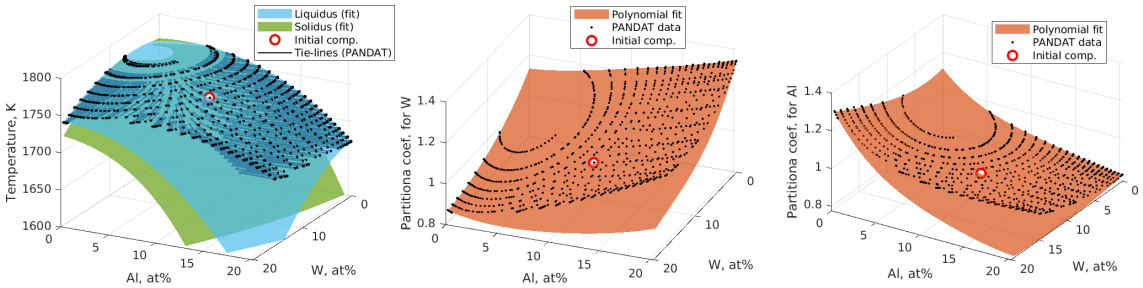

Figure 9: *Phase-diagram of Co-W-Al as predicted by the PANDAT™database (dots) and polynomial approximations (solid surface) used in this work. Figure adapted from [70].*

In addition to thermal equilibrium, chemical equilibrium must be maintained at the solidification front. For multicomponent systems, this is typically captured through the concept of partition coefficients k_J, which describe the equilibrium distribution of each solute species between the solid and liquid phases. These coefficients are defined as:

$$C_J^s = k_J C_J^l, \quad \boldsymbol{x} \in \Gamma(t), \quad J \in [1, N]\,,$$

where C_J^l and C_J^s are the concentrations of species J in the liquid and solid phases, respectively. Importantly, for general multicomponent alloys where the phase diagram is nonlinear and the liquidus/solidus surfaces are curved, the partition coefficients are not constant. Instead, they depend on the local composition of the alloy at the interface:

$$k_J = k_J\big(C_1^l, \ldots, C_N^l\big), \quad J \in [1, N]\,.$$

Mass conservation of each species at the moving interface further imposes a set of interfacial boundary conditions known as the solute-rejection equations. These conditions ensure that the solute flux in the liquid and the rate of incorporation (or rejection) of solute into the solid phase are consistent:

$$D_J^l \partial_{\boldsymbol{n}_l} C_J^l - (1 - k_J) v_{\boldsymbol{n}} C_J^l = 0, \quad \boldsymbol{x} \in \Gamma(t), \quad J \in [1, N]\,, \tag{10}$$

where D_J^l denotes the diffusivity of species J in the liquid phase. These equations capture the complex coupling between solute transport, interface motion, and phase equilibrium, and are essential for predicting microsegregation, solute trapping, and morphological stability during solidification of multicomponent alloys. Once the normal velocity at the interface is defined, the level-set evolution equation is solved as described in section 2. We refer the interested reader to [70] for the details of the numerical implementation and to [143] for a coupling of simulation of a pure substance with fluid flows.

3.2. Level-Set Simulations

A detailed accuracy analysis of the temperature, concentration, interface velocity, and interface location was conducted in [70] and is shown in Figure 10 for a ternary Co-W-Al solidification case. Errors are measured in the L^∞-norm over the full simulation time, capturing the worst-case deviation from the reference solution. The results indicate convergence rates approaching second order. This is particularly important in multicomponent alloy solidification, where strong thermal and solutal gradients interact with a moving interface. The verified accuracy supports the model's reliability for predictive simulations of complex solidification phenomena.

A practical simulation of directional solidification of a ternary Co-W-Al system is given in Figure 11. Denoting the computational domain Ω, with boundary $\partial\Omega$, it is assumed that the total heat flux is specified and the boundary is impermeable to solutes:

$$\begin{aligned} \lambda^\nu \partial_{\boldsymbol{n}_\nu} T^\nu &= g_{T^\nu}, \quad \boldsymbol{x} \in \Omega^\nu \cap \partial\Omega, \quad \nu = s, l, \\ D_J^l \partial_{\boldsymbol{n}_l} C_J^l &= 0, \qquad \boldsymbol{x} \in \Omega^l \cap \partial\Omega, \quad J \in [1, N]\,, \end{aligned} \tag{11}$$

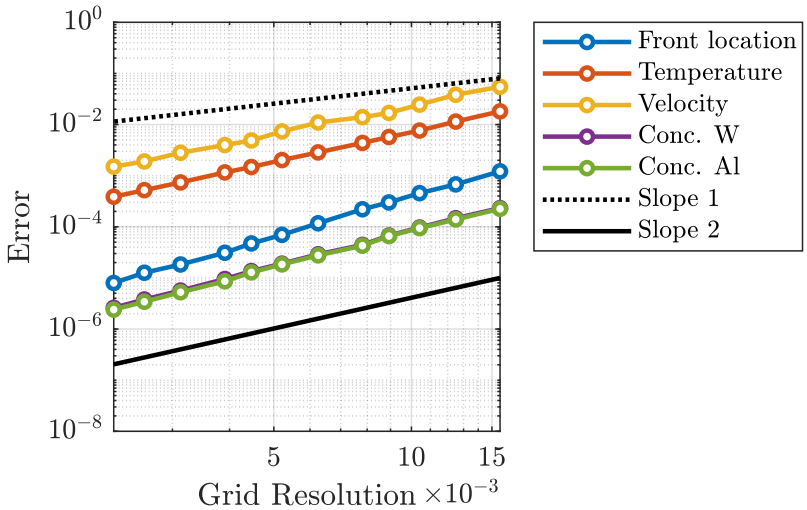

Figure 10: *Overall accuracy of the computational method in the case of stable axisymmetric solidification. Figure adapted from [70].*

where $g_{T^\nu} = g_{T^\nu}(t, \boldsymbol{x})$, $\nu = s, l$, are prescribed heat fluxes for the liquid and solid phases. The simulation investigates the influence of the thermal gradient G and the diffusion coefficient of aluminum (Al) on dendritic growth during solidification. As expected, increasing the thermal gradient leads to finer dendritic structures. The qualitative dependence of dendrite arm spacing on both G and the solidification rate R is consistent with observations in binary alloy systems. However, the quantitative details, such as the coefficients and exponents in the scaling laws, may differ due to additional complexities inherent in multicomponent systems. These include the presence of nontrivial phase diagrams, cross-diffusion effects (e.g., Onsager coupling), and unequal solute diffusivities in the liquid phase. The level-set simulation framework is particularly well-suited to capturing these effects, enabling systematic studies of how they influence microstructural evolution.

4. Application - Epitaxial Growth and the Island Dynamics Model

4.1. The Island Dynamics Model

In [86, 144], Caflisch *et al.* introduced the Island Dynamics Model (IDM) as well as its numerical approximation using the level-set method in [87, 145] and later analyzed the IDM and developed step edge boundary conditions for well-posedness [146]. The core idea of the IDM is to represent the boundary of atomic-height islands using a continuous level-set function $\phi(\boldsymbol{x}, t)$, such that Islands of heights k are represented by the level sets $\phi(\boldsymbol{x}, t) = k - 1$, and to consider a mean-field adatom density $\rho = \rho(\boldsymbol{x}, t)$. As such, the IDM achieves atomistic fidelity in the growth direction, while employing a continuum description in the lateral directions. The method also accounts for nucleation events, and other atomistic processes influencing island growth. The level-set function evolves according to the transport equation:

$$\frac{\partial \phi}{\partial t} + v_n |\nabla \phi| = 0,$$

where v_n is the interface normal velocity field, which is computed from the adatom fluxes across the island boundary from the upper $^{(k+1)}$ and lower terraces $^{(k)}$:

$$v_n = aD(\boldsymbol{n} \cdot \nabla \rho^{(k+1)} - \boldsymbol{n} \cdot \nabla \rho^{(k)}),$$

where D is the adatom diffusion coefficient and a is the lattice constant.

The adatom concentration $\rho(\boldsymbol{x}, t)$ satisfies a reaction-diffusion equation with source and sink terms:

$$\frac{\partial \rho}{\partial t} = F + D\nabla^2 \rho - \frac{dN_{\text{nuc}}}{dt},$$

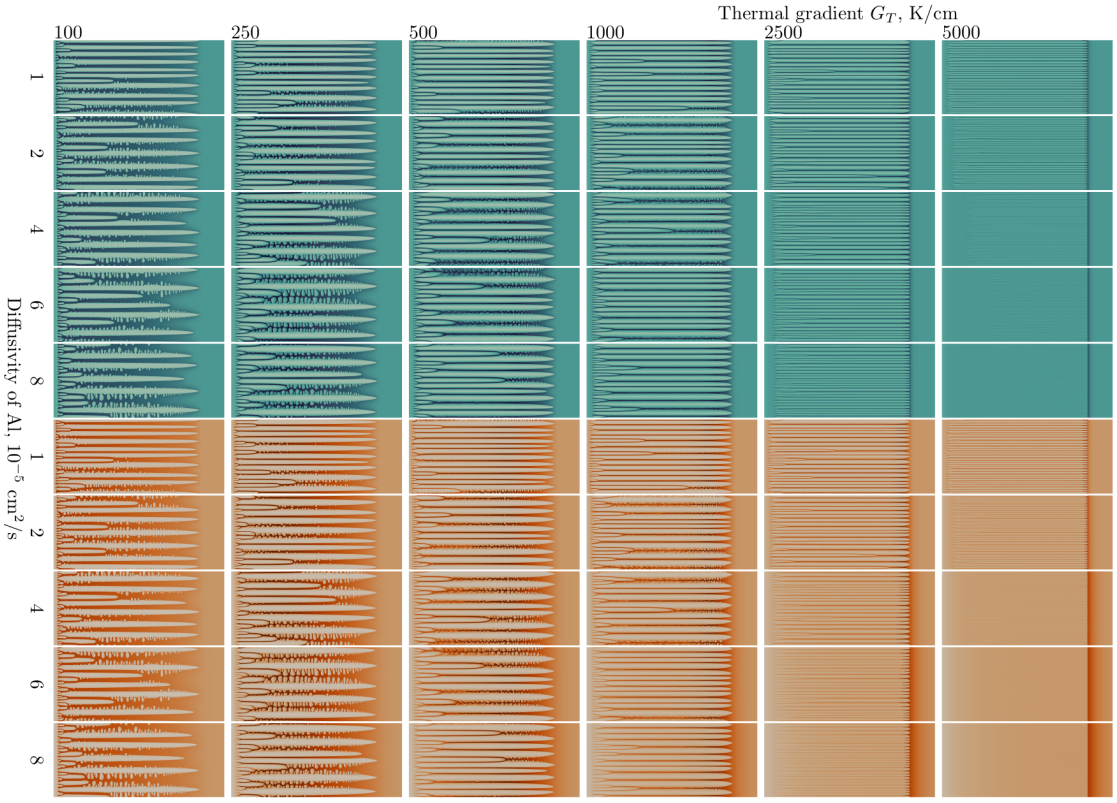

Figure 11: *Solidification microstructures obtained for values of Al diffusivity from* $D^{Al} = 10^{-5}$ *cm*^{2}*/s to* $8 \cdot 10^{-5}$ *cm*^{2}*/s and* G_T *from 100 K/cm to 5000 K/cm in case of* $L = 0.05$ *cm and* $V = 0.01$ *cm/s. Displayed in color is the concentration field of Al and W. Figure adapted from [70].*

where F is the deposition flux and the last term models the nucleation rate of new dimers assuming a probability proportional to $\langle \rho^2 \rangle$, i.e., the integral of ρ^2, and written as:

$$\frac{dN_{\text{nuc}}}{dt} = 2D\sigma_1 \langle \rho^2 \rangle,$$

where σ_1 is the capture number for nucleation [147]. The factor of 2 accounts for the capture of 2 adatoms during nucleation and the fact that dimers are assumed to be stable. In [148, 149], it was established that the capture numbers σ_s associated with islands of size s obey the scaling relation $\sigma_s/\sigma_{av} = L(s/s_{av})$, where L denotes a linear functional dependence. This representation provides a consistent framework in which the reference value σ_1 may be prescribed explicitly. This stochastic nucleation mechanism has been validated using KMC simulations [150]. Anisotropic growth can be captured by modifying v_n. A key advantage of the Island Dynamics Model is its ability to take large time steps while accurately capturing the essential physics of adatom diffusion and detachment. A notable application of this approach is presented in [151], where an Island Dynamics Model was employed to study the narrowing and sharpening of the island-size distribution as a function of strain in the submonolayer heteroepitaxial growth regime. In that work, the model is coupled to an elastic formulation based on atomistic interactions, which is solved efficiently at each simulation step.

The diffusion equation governing the adatom density ρ requires the specification of appropriate boundary conditions at island boundaries to accurately describe the underlying atomistic processes. These boundary conditions play a critical role in determining the predictive capabilities of the IDM, as they directly influence mass transport at the evolving interface. In the case where the diffusion from the upper and lower terraces are equal, the boundary condition is $\rho = \rho_{\text{eq}}$, where ρ_{eq} denotes the equilibrium adatom density. However, for most epitaxial growth, the diffusion coefficients are not equal, which promotes the growth of mounds with important practical

applications in photonic-crystal lasers, quantum dot lasers, single-photon emitters, solar cells, catalytic converters, lithography, and more. This boundary condition encapsulates the influence of the Ehrlich-Schwoebel (ES) barrier [152, 153] and serves as a key element in bridging atomistic-scale kinetics with continuum-scale morphological evolution [154, 155, 156]:

$$\nabla\rho \cdot \boldsymbol{n} + \frac{D'}{D - D'}\rho = \frac{D'}{D - D'}\rho_{\text{eq}}, \tag{12}$$

where ρ and its gradient $\nabla\rho$ are evaluated at the island boundary, D' is an atomistic rate that characterizes the energy barrier for adatom diffusion across the island edge and $\boldsymbol{n}$ is the outward normal to the boundary. In the limit $D' \to D$, the boundary condition (12) simplifies to the Dirichlet condition $\rho(\mathbf{x}) = \rho_{\text{eq}}$, as found in classical theories of step-flow growth [157, 158, 159]. The equilibrium adatom density ρ_{eq} plays a central role in defining attachment kinetics at step edges. In [160], an expression for ρ_{eq} is derived under the assumption of no Ehrlich-Schwoebel barrier, while in [137], the authors develop and implement a formulation that incorporates the effects of a finite Ehrlich-Schwoebel barrier. More generally, the value of ρ_{eq} depends on atomistic kinetic parameters, including the detachment rate and the rate of edge diffusion, as discussed in [144].

4.2. Level-Set Simulation

As an illustrative example, we report the results of level-set simulations from [161]. In the case of irreversible aggregation, corresponding to the boundary condition $\rho = 0$ at island edges, the Island Dynamics Model yields results that are in good agreement with kinetic Monte Carlo (KMC) simulations, as shown in [87]. Figure 12 illustrates this agreement by showing the evolution of the adatom density and island density as functions of surface coverage for various values of the ratio D/F. Additionally, the cluster size distribution at a final coverage of 20% is presented, further demonstrating the consistency between the IDM and atomistic simulation results. Level-set simulations have been used to find the functional form of capture numbers used in rate equations expressing the densities of islands of all sizes. The capture numbers quantify the efficiency with which an island of a given size, in a specified environment, competes for available monomers. A key advantage of the Island Density Model is its implicit incorporation of island-island correlations, thereby accounting for the geometric arrangement of islands relative to their neighbors. Notably, the capture numbers were found to exhibit a linear dependence on island size [162, 163, 164].

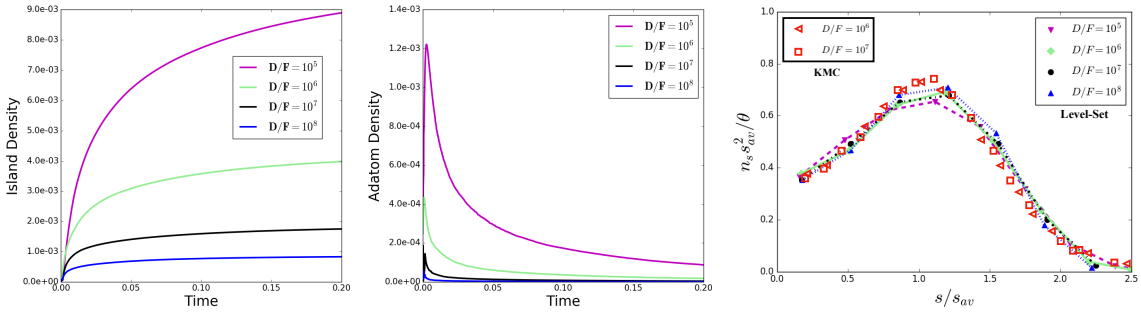

Figure 12: *The island density (left) and adatom density (center) and cluster size distribution (right) for different values of D/F in the case of the boundary condition $\rho = 0$ (irreversible aggregation). Each simulation has a final coverage of* 20%. *The KMC simulations are from [87]. Figure adapted from [161].*

Figure 13 illustrates the influence of the step-edge barrier on surface morphology during epitaxial growth. For a strong Ehrlich-Schwoebel barrier, corresponding to a small ratio $D'/D = 0.01$, the simulation exhibits the formation of well-defined mounds with a characteristic "wedding cake" structure, featuring approximately ten exposed terraces after the deposition of eleven monolayers. As D'/D increases, reflecting a reduction in the strength of the Ehrlich-Schwoebel barrier, the mounding becomes less pronounced. In the case where $D'/D = 0.95$, which is a very high ratio, the surface evolves toward a morphology consistent with near layer-by-layer growth, indicating that the suppression of interlayer transport asymmetry promotes smoother film evolution.

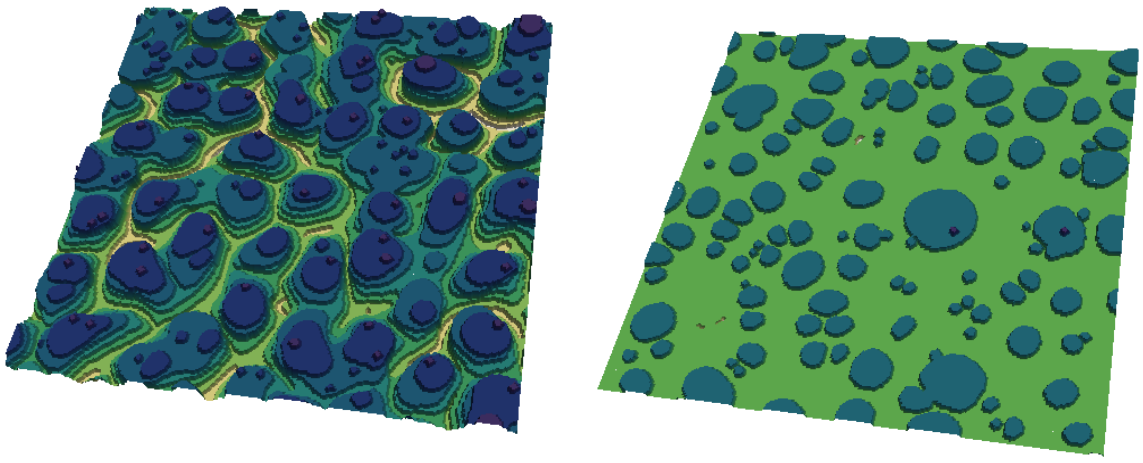

Figure 13: *Effects of the Ehrlich-Schwoebel barrier and formation of mounds with* $D'/D = 0.01$ *(left) corresponding to a strong Ehrlich-Schwoebel barrier and* $D'/D = 0.95$ *(right), corresponding to a scenario close to* $\rho(\mathbf{x}) = \rho_{\text{eq}}$*. Both simulations are at the same times. Figure adapted from [161].*

5. Conclusion and Perspective

The level-set method has emerged as a unifying computational framework for modeling free boundary problems across a wide spectrum of materials science applications. This review has synthesized its role in two contrasting yet complementary contexts: the solidification of multicomponent alloys and the mesoscale dynamics of epitaxial growth. In both application, the method's ability to maintain a sharp interface, naturally handle topological changes, and flexibly incorporate boundary conditions provides significant advantages over alternative approaches.

For alloy solidification, particularly in the context of additive manufacturing, the level-set formulation enables high-fidelity simulations of solid-liquid interfaces, capturing complex thermodynamic interactions and multi-species transport with high accuracy. It accommodates multicomponent systems and sharp-interface physics that are beyond the reach of phase-field models, especially for more than three component alloys. In the context of epitaxial growth, the Island Dynamics Model and its level-set implementation offers a continuum-scale alternative to stochastic kinetic Monte Carlo simulations, dramatically reducing computational cost while preserving physical accuracy. It efficiently models nucleation, coalescence, and step-edge kinetics, with the flexibility to incorporate key phenomena such as the Ehrlich-Schwoebel barrier through Robin-type boundary conditions. Taken together, these applications underscore the versatility and robustness of level-set methods in materials science. Their seamless integration with finite volume and finite difference discretizations, adaptive mesh refinement, and physically grounded boundary conditions makes them a powerful tool for predictive modeling and design.

Further developments in multiscale coupling, uncertainty quantification, and high-performance implementations will continue to expand the frontiers of level-set-based simulation in materials science. An especially promising direction is the integration of machine learning (ML) with level-set frameworks in materials science for designing hybrid physics-based/data-driven simulations. ML can assist in learning surrogate models for expensive forward simulations, accelerating inverse design by providing data-driven approximations of the shape-to-structure map. Recent advances in computational materials science have explored this integration to enhance modeling capabilities, improve computational efficiency, and enable data-driven materials design. One such effort is the Level-Set Learning framework, which employs reversible neural networks to identify low-dimensional parameterizations of level sets in high-dimensional spaces. This approach has proven especially effective for reducing uncertainties and avoiding overfitting when working with limited data in inverse design and predictive modeling applications [165]. Another direction is the use of hybrid inference systems that couple machine learning with classical numerical techniques to improve

curvature estimation in level-set computations or the evolution of the level-set itself. By using neural networks to refine gradient and curvature evaluations near interfaces, this approach helps mitigate numerical errors such as mass loss and surface tension computations, thereby increasing the accuracy of multiphase and interface-driven simulations [166, 167, 168, 169].

Machine learning techniques have also been integrated into the level-set framework to address Stefan problems [170], and have also been employed for operator learning in the context of inverse problems governed by diffusion-dominated dynamics [171] on fixed irregular domains. The PINN approach of [170] to the solution of the Stefan problem showed success on the prediction of planar interfaces, but it is not clear whether or not this approach will be accurate in the practical cases where dendritic structures develop. In addition, [172] pointed out that the erratic convergence behavior often observed in physics-informed neural networks (PINNs) may stem from their reliance on automatic differentiation. This concern is further supported by [173], which highlights fundamental flaws in software-based automatic differentiation, including its dependency on the network's current approximation of the solution during training. This dependency can lead to significant errors, particularly when the evolving solution is far from the true one. To address this issue, [172] proposed incorporating a discretized formulation of the governing partial differential equation (PDE), thereby bypassing automatic differentiation. Their results demonstrated that convergence improves systematically with the introduction of additional virtual grid points, yielding more accurate and stable solutions. Other fundamental work on optimization of neural networks can be found in [174, 175] and the references therein. These examples collectively highlight the emerging role of machine learning as a powerful complement to level-set methods in addressing multiscale, nonlinear, and data-intensive challenges in materials science.

Acknowledgement

Frederic Gibou was partially supported by NSF CBET-EPSRC 2054894 and ACS PRF 66673-ND9. Ron Fedkiw was partially by ONR N00014-24-1-2644, ONR N00014-21-1-2771, and ONR N00014-19-1-2285. Russel Caflisch was partially supported by KAUST ORFS-2023-OFP-5538.2. Stanley Osher was partially supported by ONR N00014-20-1-2787, NSF-2208272, STROBE NSF-1554564, NSF 234525 and by Air Force Office of Scientific Research (AFOSR) MURI FA9550-18-502.

References

[1] S. Osher and J.A. Sethian. Fronts propagating with curvature-dependent speed: Algorithms based on hamilton-jacobi formulations. J. Comput. Phys., 79:12–49, 1988.

[2] M. Sussman, P. Smereka, and S. Osher. A level set approach for computing solutions to incompressible two-phase flow. Journal of Computational Physics, 114:146–159, 1994.

[3] Mark Sussman, Kenneth M. Smith, M. Yousuff Hussaini, Masaru Ohta, and Rui Zhi-Wei. A sharp interface method for incompressible two-phase flows. Journal of Computational Physics, 221(2):469–505, 2007.

[4] Mark Sussman, Ebrahim Fatemi, Peter Smereka, and Stanley Osher. An improved level set method for incompressible two-phase flows. Computers & Fluids, 27(5–6):663–680, 1998.

[5] Mark Sussman, Ann S. Almgren, John B. Bell, Phillip Colella, Louis H. Howell, and M. Welcome. An adaptive level set approach for incompressible two-phase flows. Journal of Computational Physics, 148(1):81–124, 1999.

[6] Y.C. Chang, T.Y. Hou, B. Merriman, and S. Osher. A level set formulation of eulerian interface capturing methods for incompressible fluid flows. Journal of Computational Physics, 124(2):449–464, 1996.

[7] D. Enright, D. Nguyen, F. Gibou, and R. Fedkiw. Using the particle level set method and a second order accurate pressure boundary condition for free surface flows. In Proc. 4th ASME-JSME Joint Fluids Eng. Conf., number FEDSM2003–45144. ASME, 2003.

[8] Thomas Y. Hou, Zhiming Li, Stanley Osher, and Hongkai Zhao. A hybrid method for moving interface problems with application to the hele–shaw flow. Journal of Computational Physics, 134(2):236–252, 1997.

[9] H.S. Udaykumar, R. Mittal, P. Rampunggoon, and A. Khanna. A sharp interface cartesian grid method for simulating flows with complex moving boundaries. Journal of Computational Physics, 174(1):345–380, 2001.

[10] Duc Nguyen, Frederic Gibou, and Ronald Fedkiw. A fully conservative ghost fluid method and stiff detonation waves. In 12th International Detonation Symposium, San Diego, CA, 2002.

[11] Frédéric Gibou and Chohong Min. Efficient symmetric positive definite second-order accurate monolithic solver for fluid/solid interactions. Journal of Computational Physics, 231(8):3246–3263, 2012.

[12] Rachel Caiden, Ronald P. Fedkiw, and Chris Anderson. A numerical method for two-phase flow consisting of separate compressible and incompressible regions. J. Comput. Phys., 166(1):1 – 27, 2001.

[13] Yen Ting Ng, Chohong Min, and Frédéric Gibou. An efficient fluid–solid coupling algorithm for single-phase flows. Journal of Computational Physics, 228(23):8807–8829, 2009.

[14] T. Tasdizen, R. Whitaker, P. Burchard, and S. Osher. Geometric surface smoothing via anisotropic diffusion of normals. In Proceedings of IEEE Visualization 2002 (VIS 2002), pages 125–132. IEEE, 2002.

[15] S Osher and N Paragios. Geometric Level Set Methods in Imaging, Vision, and Graphics. Springer-Verlag, 2003.

[16] Stanley Osher and Richard Tsai. Review article: Level Set Methods and Their Applications in Image Science. Communications in Mathematical Sciences, 1(4):1–20, December 2003.

[17] E. Guendelman, A. Selle, F. Losasso, and R. Fedkiw. Coupling water and smoke to thin deformable and rigid shells. ACM Trans. Graph. (SIGGRAPH Proc.), 24(3), 2005.

[18] D. Enright, S. Marschner, and R. Fedkiw. Animation and rendering of complex water surfaces. ACM Trans. Graph. (SIGGRAPH Proc.), 21(3):736–744, 2002.

[19] Frank Losasso, Ron Fedkiw, and Stanley Osher. Spatially Adaptive Techniques for Level Set Methods and Incompressible Flow. Computers and Fluids, 35:995–1010, 2006.

[20] N. Foster and R. Fedkiw. Practical animation of liquids. In Proc. of ACM SIGGRAPH 2001, pages 23–30, 2001.

[21] Frank Losasso, Frederic Gibou, and Ron Fedkiw. Simulating water and smoke with an octree data structure. ACM Trans. Graph. (SIGGRAPH Proc.), pages 457–462, 2004.

[22] Duc Q. Nguyen, Ronald P. Fedkiw, and Myungjoo Kang. A boundary condition capturing method for incompressible flame discontinuities. Journal of Computational Physics, 172(1):71–98, 2001.

[23] Mridul Aanjaneya, Saket Patkar, and Ronald Fedkiw. A monolithic mass tracking formulation for bubbles in incompressible flow. Journal of Computational Physics, 247:17 – 61, 2013.

[24] Martin Burger, Stanley J. Osher, and Eli Yablonovitch. Inverse problem techniques for the design of photonic crystals. IEICE Transactions on Electronics, 87(3):258–265, 2004.

[25] Hong-Kai Zhao, Stanley Osher, and Ronald Fedkiw. Fast surface reconstruction using the level set method. In Proceedings of the IEEE Workshop on Variational and Level Set Methods in Computer Vision, pages 194–201. IEEE, 2001.

[26] Stanley J. Osher and Fadil Santosa. Level set methods for optimization problems involving geometry and constraints: I. frequencies of a two-density inhomogeneous drum. Journal of Computational Physics, 171(1):272–288, 2001.

[27] Grégoire Allaire, François Jouve, and Anca-Maria Toader. A level-set method for shape optimization. Comptes Rendus Mathematique, 334(12):1125–1130, 2002.

[28] Grégoire Allaire, François Jouve, and Anca-Maria Toader. Structural optimization using sensitivity analysis and a level-set method. Journal of Computational Physics, 194(1):363–393, 2004.

[29] Rochishnu Chowdhury, Raphael Egan, Daniil Bochkov, and Frederic Gibou. Efficient calculation of fully resolved electrostatics around large biomolecules. Journal of Computational Physics, 448:110718, 2022.

[30] Raphael Egan and Frederic Gibou. Fast and scalable algorithms for constructing solvent-excluded surfaces of large biomolecules. Journal of Computational Physics, 374:91–120, 2018.

[31] Gaddiel Ouaknin, Nabil Laachi, Daniil Bochkov, Kris Delaney, Glenn Fredrickson, and Frederic Gibou. Functional level-set derivative for self consistent field theory. J. Comp. Phys., 345:168–185, 2017.

[32] Gaddiel Ouaknin, Nabil Laachi, Kris Delaney, Glenn Fredrickson, and Frederic Gibou. Shape optimization for dsa. In Alternative Lithographic Technologies VIII, volume 9777, pages 168–178. SPIE, 2016.

[33] Gaddiel Ouaknin, Nabil Laachi, Kris Delaney, Glenn H Fredrickson, and Frederic Gibou. Self-consistent field theory simulations of polymers on arbitrary domains. Journal of Computational Physics, 327:168–185, 2016.

[34] Gaddiel Ouaknin, Nabil Laachi, Daniil Bochkov, Kris Delaney, Glenn H Fredrickson, and Frederic Gibou. Functional level-set derivative for a polymer self consistent field theory hamiltonian. Journal of Computational Physics, 345:207–223, 2017.

[35] Gaddiel Y Ouaknin, Nabil Laachi, Kris Delaney, Glenn H Fredrickson, and Frederic Gibou. Level-set strategy for inverse dsa-lithography. Journal of Computational Physics, 375:1159–1178, 2018.

[36] Daniil Bochkov and Frederic Gibou. A non-parametric gradient-based shape optimization approach for solving inverse problems in directed self-assembly of block copolymers. Communications on Applied Mathematics and Computation, 6(2):1472–1489, 2024.

[37] Martin Burger and Stanley J. Osher. A survey on level set methods for inverse problems and optimal design. European Journal of Applied Mathematics, 16(2):263–301, 2005.

[38] Mark Sussman. A second order coupled level set and volume-of-fluid method for computing growth and collapse of vapor bubbles. Journal of Computational Physics, 187(1):110–136, 2003.

[39] Mark Sussman and Elbridge Gerry Puckett. A coupled level set and volume-of-fluid method for computing 3d and axisymmetric incompressible two-phase flows. Journal of Computational Physics, 162(2):301–337, 2000.

[40] Douglas Enright, Ronald Fedkiw, Joel Ferziger, and Ian Mitchell. A hybrid particle level set method for improved interface capturing. Journal of Computational Physics, 183(1):83–116, 2002.

[41] S. Osher and R. Fedkiw. Level Set Methods and Dynamic Implicit Surfaces. Springer-Verlag, New York, NY, 2002.

[42] J. A. Sethian. Level set methods and fast marching methods, volume 3 of Cambridge Monographs on Applied and Computational Mathematics. Cambridge University Press, Cambridge, 2 edition, 1999. Evolving interfaces in computational geometry, fluid mechanics, computer vision, and materials science.

[43] Stanley Osher and Ronald P. Fedkiw. Level set methods: An overview and some recent results. Journal of Computational Physics, 169(2):463–502, 2001.

[44] Frederic Gibou, Ronald Fedkiw, and Stanley Osher. A review of level-set methods and some recent applications. Journal of Computational Physics, 353:82–109, 2018.

[45] Stanley Osher, Ronald Fedkiw, and Krzysztof Piechor. Level set methods and dynamic implicit surfaces. Applied Mechanics Reviews, 57(3):B15–B15, 2004.

[46] Dong Dong Gu, Wilhelm Meiners, Konrad Wissenbach, and Reinhart Poprawe. Laser additive manufacturing of metallic components: materials, processes and mechanisms. International materials reviews, 57(3):133–164, 2012.

[47] TM Pollock, AJ Clarke, and SS Babu. Design and tailoring of alloys for additive manufacturing. Metallurgical and Materials Transactions A, 51(12):6000–6019, 2020.

[48] Bhaskar Dutta, Sudarsanam Babu, and Bradley H Jared. Science, technology and applications of metals in additive manufacturing. Elsevier, 2019.

[49] Tarasankar DebRoy, HL Wei, JS Zuback, T Mukherjee, JW Elmer, JO Milewski, Allison Michelle Beese, A de Wilson-Heid, A De, and W Zhang. Additive manufacturing of metallic components–process, structure and properties. Progress in Materials Science, 92:112–224, 2018.

[50] William J Sames, FA List, Sreekanth Pannala, Ryan R Dehoff, and Sudarsanam Suresh Babu. The metallurgy and processing science of metal additive manufacturing. International materials reviews, 61(5):315–360, 2016.

[51] Suman Das, David L Bourell, and SS Babu. Metallic materials for 3d printing. Mrs Bulletin, 41(10):729–741, 2016.

[52] Narendran Raghavan, Ryan Dehoff, Sreekanth Pannala, Srdjan Simunovic, Michael Kirka, John Turner, Neil Carlson, and Sudarsanam S Babu. Numerical modeling of heat-transfer and the influence of process parameters on tailoring the grain morphology of in718 in electron beam additive manufacturing. Acta Materialia, 112:303–314, 2016.

[53] Wilfried Kurz, C Bezencon, and M Gäumann. Columnar to equiaxed transition in solidification processing. Science and technology of advanced materials, 2(1):185, 2001.

[54] K Reuther and M Rettenmayr. Perspectives for cellular automata for the simulation of dendritic solidification–a review. Computational materials science, 95:213–220, 2014.

[55] Alain Karma. Phase-field formulation for quantitative modeling of alloy solidification. Physical Review Letters, 87(11):115701, 2001.

[56] Seong Gyoon Kim. A phase-field model with antitrapping current for multicomponent alloys with arbitrary thermodynamic properties. Acta Materialia, 55(13):4391–4399, 2007.

[57] Ingo Steinbach. Phase-field models in materials science. Modelling and simulation in materials science and engineering, 17(7):073001, 2009.

[58] Lijian Tan and Nicholas Zabaras. A level set simulation of dendritic solidification of multicomponent alloys. Journal of Computational Physics, 221(1):9–40, 2007.

[59] S. Chen, B. Merriman, S. Osher, and P. Smereka. A simple level set method for solving stefan problems. Journal of Computational Physics, 135(1):8–29, 1997.

[60] H.S Udaykumar, S Marella, and S Krishnan. Sharp-interface simulation of dendritic growth with convection: benchmarks. International Journal of Heat and Mass Transfer, 46(14):2615 – 2627, 2003.

[61] Joseph Papac, Asdis Helgadottir, Christian Ratsch, and Frederic Gibou. A level set approach for diffusion and Stefan-type problems with Robin boundary conditions on Quadtree/Octree adaptive Cartesian grids. J. Comput. Phys., 233:241–261, 2013.

[62] Han Chen, Chohong Min, and Frederic Gibou. A supra-convergent finite difference scheme for the poisson and heat equations on irregular domains and non-graded adaptive cartesian grids. Journal of Scientific Computing, 31:19–60, 2007.

[63] Frédéric Gibou, Ronald Fedkiw, Russel Caflisch, and Stanley Osher. A level set approach for the numerical simulation of dendritic growth. Journal of Scientific Computing, 19:183–199, 2003.

[64] Yi Yang and HS Udaykumar. Sharp interface cartesian grid method iii: Solidification of pure materials and binary solutions. Journal of Computational Physics, 210(1):55–74, 2005.

[65] Maxime Theillard, Frédéric Gibou, and Tresa Pollock. A sharp computational method for the simulation of the solidification of binary alloys. J. Sci. Comput., 63(2):330–354, 2015.

[66] James A. Sethian and John Strain. Crystal growth and dendritic solidification. Journal of Computational Physics, 98(2):231–253, 1992.

[67] A Mayo. The Fast Solution of Poisson's and the Biharmonic Equations on Irregular Regions. SIAM J. Numer. Anal., 21:285–299, 1984.

[68] Frederic Gibou, Ron Fedkiw, Li-Tien Cheng, and Myngjoo Kang. A second-order accurate symmetric discretization of the Poisson equation on irregular domains. J. Comput. Phys., 176:205–227, 2002.

[69] Frédéric Gibou and Ronald Fedkiw. A fourth order accurate discretization for the laplace and heat equations on arbitrary domains, with applications to the stefan problem. Journal of Computational Physics, 202(2):577–601, 2005.

[70] Daniil Bochkov, Tresa Pollock, and Frederic Gibou. A numerical method for sharp-interface simulations of multicomponent alloy solidification. Journal of Computational Physics, 494:112494, 2023.

[71] A. Pimpinelli and J. Villain. Physics of Crystal Growth. Cambridge University Press, Cambridge, 1999.

[72] Harald Brune. Microscopic view of epitaxial metal growth: nucleation and aggregation. Surface Science Reports, 31(3-4):121–229, 1998.

[73] N. Cheimarios. Monte carlo and kinetic monte carlo models for deposition processes. Frontiers in Physics, 9:631918, 2021.

[74] S. Sakthinathan, G. A. Meenakshi, S. Vinothini, C.-L. Yu, C.-L. Chen, T.-W. Chiu, and N. Vittayakorn. A review of thin-film growth, properties, applications, and future prospects. Processes, 13(2):587, 2025.

[75] Russel Caflisch. Multiscale modeling for epitaxial growth. In Axel Voigt, editor, Multiscale Modeling of Epitaxial Growth Processes, pages 55–108. Birkhäuser, Boston, MA, 2006.

[76] Dionisios G. Vlachos. A review of multiscale analysis: examples from systems biology, materials growth, and other reacting systems. Chemical Engineering Science, 60(1):7–16, 2005.

[77] J. A. Venables, G. D. T. Spiller, and M. Hanbücken. Nucleation and growth of thin films. Reports on Progress in Physics, 47(4):399–459, 1984.

[78] J. W. Evans, P. A. Thiel, and M. C. Bartelt. Morphological evolution during epitaxial thin film growth: Formation of 2d islands and 3d mounds. Surface Science Reports, 61(1-2):1–128, 2006.

[79] P. A. Maksym. Fast monte carlo simulation of mbe growth. Semiconductor Science and Technology, 3:594, 1988.

[80] Jason P DeVita, Leonard M Sander, and Peter Smereka. Multiscale kinetic monte carlo algorithm for simulating epitaxial growth. Physical Review B—Condensed Matter and Materials Physics, 72(20):205421, 2005.

[81] Corbett C Battaile and David J Srolovitz. Kinetic monte carlo simulation of chemical vapor deposition. Annual Review of Materials Research, 32(1):297–319, 2002.

[82] K. Reuter and M. Scheffler. First-principles kinetic monte carlo simulations for heterogeneous catalysis: Application to the co oxidation at ruo2(110). Physical Review B, 73:045433, 2006.

[83] Huijun Jiang and Zhonghuai Hou. Large-scale epitaxial growth kinetics of graphene: a kinetic monte carlo study. The Journal of Chemical Physics, 143(8), 2015.

[84] Xuejiang Chen, Xinyao Zhang, and Wensen Ai. Kinetic monte carlo study on the effect of growth conditions on the epitaxial growth of 3c-sic (0001) vicinal surface. Journal of Vacuum Science Technology A, 42, 01 2024.

[85] R.E. Caflisch, M.F. Gyure, B. Merriman, S. Osher, C. Ratsch, D.D. Vvedensky, and J.J. Zinck. Island dynamics and the level set method for epitaxial growth. Applied Mathematics Letters, 12:13, 1999.

[86] M. F. Gyure, C. Ratsch, B. Merriman, R. E. Caflisch, S. Osher, J. J. Zinck, and D. D. Vvedensky. Level-set methods for the simulation of epitaxial phenomena. Physical Review E, 58(6):R6927–R6930, 1998.

[87] Susan Chen, Barry Merriman, Myungjoo Kang, Russel E. Caflisch, Christian Ratsch, Li-Tien Cheng, Mark Gyure, Ronald P. Fedkiw, Christopher Anderson, and Stanley Osher. A level set method for thin film epitaxial growth. Journal of Computational Physics, 167(2):475–500, 2001.

[88] Chi-Wang Shu. Efficient implementation of essentially non-oscillatory schemes , ii. Journal of Computational Physics, 78:32–78, 1989.

[89] C.-W. Shu and S. Osher. Efficient implementation of essentially non-oscillatory shock capturing schemes ii. Journal of Computational Physics, 83:32–78, 1989.

[90] X.-D. Liu, S. Osher, and T. Chan. Weighted essentially non-oscillatory schemes. Journal of Computational Physics, 126:202–212, 1996.

[91] G.-S. Jiang and D. Peng. Weighted eno schemes for hamilton-jacobi equations. SIAM Journal on Scientific Computing, 21:2126–2143, 2000.

[92] J. Tsitsiklis. Efficient algorithms for globally optimal trajectories. IEEE Transactions on Automatic Control, 40:1528–1538, 1995.

[93] J. Sethian. Fast marching methods. SIAM Review, 41:199–235, 1999.

[94] Hongkai Zhao. A fast sweeping method for eikonal equations. Mathematics of Computation, 74:603–627, 2004.

[95] Y.-H. Tsai, L.-T. Cheng, and S. Osher. Fast sweeping algorithms for a class of hamilton-jacobi equations. SIAM Journal on Numerical Analysis, 41(2):673–694, 2003.

[96] Hongkai Zhao. Parallel implementations of the fast sweeping method. Journal of Computational Mathematics, 25:421–429, 2007.

[97] Miles Detrixhe, Frederic Gibou, and Chohong Min. A parallel fast sweeping method for the eikonal equation. Journal of Computational Physics, 237:46–55, 2013.

[98] Miles Detrixhe and Frederic Gibou. Hybrid massively parallel fast sweeping method for static hamilton-jacobi equations. In preparation, 2014.

[99] Yen-Hsi Richard Tsai. Rapid and accurate computation of the distance function using grids. Journal of Computational Physics, 178(1):175–195, 2002.

[100] Per-Eric Danielsson. Euclidean distance mapping. Computer Graphics and Image Processing, 14(3):227–248, 1980.

[101] Gunilla Borgefors. Distance transformations in digital images. Computer Vision, Graphics, and Image Processing, 34(3):344–371, 1986.

[102] Mark Sussman and Elham Fatemi. An efficient, interface-preserving level set re-distancing algorithm and its application to interfacial incompressible fluid flow. SIAM Journal on Scientific Computing, 20(4):1165–1191, 1999.

[103] Chohong Min. On reinitializing level set functions. Journal of Computational Physics, 229(8):2764–2772, 2010.

[104] Jerome Darbon and Stanley Osher. Algorithms for overcoming the curse of dimensionality for certain hamiltonâjacobi equations arising in control theory and elsewhere. Research in the Mathematical Sciences, 3:19, 2016.

[105] Yat Tin Chow, Jérôme Darbon, Stanley Osher, and Wotao Yin. Algorithm for overcoming the curse of dimensionality for time-dependent non-convex hamilton-jacobi equations arising from optimal control and differential games problems. Journal of Scientific Computing, 73(2-3):617–643, 2017.

[106] Mohammad Mirzadeh, Arthur Guittet, Carsten Burstedde, and Frederic Gibou. Parallel level-set methods on adaptive tree-based grids. J. Comput. Phys., 322:345 – 364, 2016.

[107] Chohong Min, Frédéric Gibou, and Hector D Ceniceros. A supra-convergent finite difference scheme for the variable coefficient poisson equation on non-graded grids. Journal of Computational Physics, 218(1):123–140, 2006.

[108] Chohong Min and Frederic Gibou. A second order accurate level set method on non-graded adaptive cartesian grids. Journal of Computational Physics, 225(1):300–321, 2007.

[109] Mohammad Mirzadeh, Maxime Theillard, and Frederic Gibou. A second-order discretization of the nonlinear Poisson Boltzmann equation over irregular geometries using non-graded adaptive cartesian grids. Journal of Computational Physics, 230(5):2125–2140, 2011.

[110] Maxime Theillard, Landry Fokoua Djodom, Jean-Leopold Vie, and Frederic Gibou. A second-order sharp numerical method for solving the linear elasticity equations on irregular domains and adaptive grids–application to shape optimization. Journal of Computational Physics, 233:430–448, 2013.

[111] M. Mirzadeh, M. Theillard, A. Helgadottir, D. Boy, and F. Gibou. An adaptive, finite difference solver for the nonlinear poisson-boltzmann equation with applications to biomolecular computations. Communications in Computational Physics, 13(1):150–173, 2012.

[112] Asdis Helgadottir and Frederic Gibou. A poisson-boltzmann solver on irregular domains with neumann or robin boundary conditions on non-graded adaptive grid. Journal of Computational Physics, 230:3830–3848, 2011.

[113] Chohong Min and Frederic Gibou. Geometric integration over irregular domains with application to level-set methods. J. Comput. Phys., 226:1432–1443, 2007.

[114] Arthur Guittet, Maxime Theillard, and FrÃ©dÃ©ric Gibou. A stable projection method for the incompressible navierâstokes equations on arbitrary geometries and adaptive quad/octrees. Journal of Computational Physics, 292:215–238, 2015.

[115] Arthur Guittet, Clair Poignard, and Frederic Gibou. A voronoi interface approach to cell aggregate electropermeabilization. Journal of Computational Physics, 332:143–159, 2017.

[116] Frederic Gibou, Chohong Min, and Ronald Fedkiw. High resolution sharp computational methods for elliptic and parabolic problems in complex geometries. Journal of Scientific Computing, 54:369–413, 2013.

[117] Chohong Min and Frederic Gibou. A second order accurate projection method for the incompressible navier-stokes equations on non-graded adaptive grids. Journal of Computational Physics, 219(2):912–929, December 2006.

[118] Han Chen, Chohong Min, and Frédéric Gibou. A numerical scheme for the stefan problem on adaptive cartesian grids with supralinear convergence rate. Journal of Computational Physics, 228(16):5803–5818, 2009.

[119] Carsten Burstedde, Lucas C Wilcox, and Omar Ghattas. p4est: Scalable algorithms for parallel adaptive mesh refinement on forests of octrees. SIAM Journal on Scientific Computing, 33(3):1103–1133, 2011.

[120] M. Berger and P. Colella. Local adaptive mesh refinement for shock hydrodynamics. Journal of Computational Physics, 82:64–84, 1989.

[121] Ronald P. Fedkiw, Tariq Aslam, Barry Merriman, and Stanley Osher. A non-oscillatory eulerian approach to interfaces in multimaterial flows (the ghost fluid method). Journal of Computational Physics, 152(2):457–492, 1999.

[122] Ronald P. Fedkiw, Antonio Marquina, and Barry Merriman. An isobaric fix for the overheating problem in multimaterial compressible flows. Journal of Computational Physics, 148(2):545–578, 1999.

[123] Ronald P. Fedkiw. Coupling an eulerian fluid calculation to a lagrangian solid calculation with the ghost fluid method. Journal of Computational Physics, 175(1):200–224, 2002.

[124] Ronald P. Fedkiw, Tariq Aslam, and Shaojie Xu. The ghost fluid method for deflagration and detonation discontinuities. Journal of Computational Physics, 154(2):393–427, 1999.

[125] Daniil Bochkov and Frederic Gibou. Solving elliptic interface problems with jump conditions on cartesian grids. Journal of Computational Physics, 407:109269, 2020.

[126] Xu-Dong Liu, Ronald P. Fedkiw, and Myungjoo Kang. A boundary condition capturing method for poissonâs equation on irregular domains. Journal of Computational Physics, 160(1):151–178, 2000.

[127] Robert E. English, Lin Qiu, Ye Yu, and Ronald Fedkiw. Chimera grids for water simulation. In ACM SIGGRAPH/Eurographics Symposium on Computer Animation (SCA), 2013.

[128] Arthur Guittet, Mathieu Lepilliez, Sebastien Tanguy, and FrÃ©dÃ©ric Gibou. Solving elliptic problems with discontinuities on irregular domains â the voronoi interface method. Journal of Computational Physics, 298:747–765, 2015.

[129] Raphael Egan and Frederic Gibou. xGFM: Recovering convergence of fluxes in the ghost fluid method. Journal of Computational Physics, 409:109351, 2020.

[130] Yen Ting Ng, Han Chen, Chohong Min, and Frédéric Gibou. Guidelines for poisson solvers on irregular domains with dirichlet boundary conditions using the ghost fluid method. Journal of Scientific Computing, 41:300–320, 2009.

[131] Armando Coco and Giovanni Russo. Finite-difference ghost-point multigrid methods on Cartesian grids for elliptic problems in arbitrary domains. J. Comput. Phys., 241:464–501, 2013.

[132] Olivier Gallinato and Clair Poignard. Superconvergent Cartesian methods for Poisson type equations in 2d – domains. Technical report, 2015.

[133] Olivier Gallinato and Clair Poignard. Superconvergent second order Cartesian method for solving free boundary problem for invadopodia formation. J. Comp. Phys., 339:412–431, 2017.

[134] Z Jomaa and C Macaskill. Numerical solution of the 2-D Poisson equation on an irregular domain with Robin boundary conditions. Proceedings of the 14th Biennial Computational Techniques and Applications Conference, 50:1–10, 2008.

[135] Z. Jomaa and C. Macaskill. The Shortley-Weller embedded finite-difference method for the 3d Poisson equation with mixed boundary conditions. J. Comp. Phys., 229(10):3675–3690, 2010.

[136] François Bouchon and Gunther H. Peichl. A second-order immersed interface technique for an elliptic Neumann problem. Numerical Methods for Partial Differential Equations, 23(2):400–420, mar 2007.

[137] Joseph Papac, Frederic Gibou, and Christian Ratsch. Efficient symmetric discretization for the Poisson, heat and Stefan-type problems with Robin boundary conditions. J. Comput. Phys., 229:875–889, 2010.

[138] Chohong Min and Frederic Gibou. Robust second-order accurate discretizations of the multi-dimensional Heaviside and Dirac delta functions. J. Comput. Phys., 227(22):9686–9695, November 2008.

[139] Raphael Egan and Frederic Gibou. Geometric discretization of the multidimensional dirac delta distribution with application to the poisson equation with singular source terms. Journal of Computational Physics, 346:71–90, 2017.

[140] Victoria Arias, Daniil Bochkov, and Frederic Gibou. Poisson equations in irregular domains with Robin boundary conditions - solver with second-order accurate gradients. J. Comput. Phys., 365:1–6, 2018.

[141] H. Johansen and P. Colella. A Cartesian grid embedded boundary method for Poisson equation on irregular domains. J. Comput. Phys., 147:60–85, 1998.

[142] Daniil Bochkov and Frederic Gibou. Solving poisson-type equations with robin boundary conditions on piecewise smooth interfaces. Journal of Computational Physics, 376:1156–1198, 2019.

[143] Elyce Bayat, Raphael Egan, Daniil Bochkov, Alban Sauret, and Frederic Gibou. A sharp numerical method for the simulation of stefan problems with convective effects. Journal of Computational Physics, 471:111627, 2022.

[144] R.E. Caflisch, M.F. Gyure, B. Merriman, S. Osher, C. Ratsch, D.D. Vvedensky, and J.J. Zinck. Island dynamics and the level set method for epitaxial growth. Applied Mathematics Letters, 12:13, 1999.

[145] C. Ratsch, M. F. Gyure, R. E. Caflisch, F. Gibou, M. Petersen, M. Kang, J. Garcia, and D. D. Vvedensk. Level-set method for island dynamics in epitaxial growth. Phys. Rev. B, 65:195403, 2002.

[146] Russel E. Caflisch and Bo Li. Analysis of island dynamics in epitaxial growth of thin films. Multiscale Modeling & Simulation, 1(1):150–171, 2003.

[147] G. S. Bales and D. C. Chrzan. Dynamics of irreversible island growth during submonolayer epitaxy. Physical Review B, 50:6057–6067, 1994.

[148] Frederic Gibou, Christian Ratsch, Suzan Chen, Mark Gyure, and Russel Caflisch. Rate equations and capture numbers with implicit island correlations. Physical Review B, 63:115401, 2001.

[149] Frederic Gibou, Christian Ratsch, and Russel Caflisch. Capture numbers in rate equations and scaling laws for epitaxial growth. Physical Review B, 67:155403, 2003.

[150] C. Ratsch, M.F. Gyure, S. Chen, M. Kang, and D.D. Vvedensky. Fluctuation and Scaling in Aggregation Phenomena. Phys. Rev. B, 61:R10598, 2000.

[151] C. Ratsch, J. DeVita, and P. Smereka. Level-set simulation for the strain-driven sharpening of the island-size distribution during submonolayer heteroepitaxial growth. Phys. Rev. B, 80:155309, Oct 2009.

[152] G. Ehrlich and F. Hudda. Atomic view of surface self-diffusion: Tungsten on tungsten. J. Chem. Phys., 44:1039, 1966.

[153] R. L. Schwoebel and E. J. Shipsey. Step motion on crystal surfaces. J. Appl. Phys., 37:3682–3686, 1966.

[154] A. A. Chernov. The spiral growth of crystals. Soviet Phys. Uspekhi, 4:116–148, 1961.

[155] J. Villain. Continuum models of crystal growth from atomic beams with and without desorption. J. Phys. (France) I, 1, 1991.

[156] H.-C. Jeong and E. D. Williams. Steps on surfaces: experiment and theory. Surf. Sci. Rep, 34:171–294, 1999.

[157] W. K. Burton, N. Cabrera, and F. C. Frank. The growth of crystals and the equilibrium structure of their surfaces. Philosophical Transactions of the Royal Society of London. Series A, 243:299–358, 1951.

[158] A Pimpinelli and J Villain. Physics of Crystal Growth. Cambridge University Press, Cambridge, UK, 1999.

[159] J. Lu, J.-G. Liu, and D. Margetis. Emergence of step flow from an atomistic scheme of epitaxial growth in 1 + 1 dimensions. Physical Review E, 91:032403, 2015.

[160] R. E. Caflisch, W. E, M. F. Gyure, B. Merriman, and C. Ratch. Kinetic model for a step edge in epitaxial growth. Phys. Rev. E, 59:6879–6887, 1999.

[161] Pouria Mistani, Arthur Guittet, Daniil Bochkov, Joshua Schneider, Dionisios Margetis, Christian Ratsch, and Frederic Gibou. The island dynamics model on parallel quadtree grids. Journal of Computational Physics, 361:150–166, 2018.

[162] Frederic Gibou, Christian Ratsch, Suzan Chen, Mark Gyure, and Russel Caflisch. Rate Equations and Capture Numbers with Implicit Island Correlations. Phys. Rev. B., 63:115401, 2001.

[163] Frederic Gibou, Christian Ratsch, and Russel Caflisch. Capture numbers in rate equations and scaling laws for epitaxial growth. Phys. Rev. B., 67:155403, 2003.

[164] D Vvedensky, C Ratsch, F Gibou, and R Vardavas. Singularities and spatial fluctuations in submonolayer epitaxy. Phys. Rev. Lett., 90:189601, 2003.

[165] Oak Ridge National Laboratory. Level set learning: Reducing uncertainties in function approximation, 2022. https://www.ornl.gov/research-highlight/level-set-learning-reducing-uncertainties-function-approximation.

[166] Luis Ángel Larios-Cárdenas and Frédéric Gibou. Machine learning algorithms for three-dimensional mean-curvature computation in the level-set method. Journal of Computational Physics, 478:111995, 2023.

[167] Luis Ángel Larios-Cárdenas and Frederic Gibou. A hybrid inference system for improved curvature estimation in the level-set method using machine learning. Journal of Computational Physics, 463:111291, 2022.

[168] Luis Ángel Larios-Cárdenas and Frederic Gibou. Error-correcting neural networks for semi-lagrangian advection in the level-set method. Journal of Computational Physics, 471:111623, 2022.

[169] Luis Ángel Larios-Cárdenas and Frederic Gibou. A deep learning approach for the computation of curvature in the level-set method. SIAM Journal on Scientific Computing, 43(3):A1754–A1779, 2021.

[170] Sifan Wang and Paris Perdikaris. Deep learning of free boundary and stefan problems. Journal of Computational Physics, 428:109914, 2021.

[171] Samira Pakravan, Pouria A Mistani, Miguel A Aragon-Calvo, and Frederic Gibou. Solving inverse-pde problems with physics-aware neural networks. Journal of Computational Physics, 440:110414, 2021.

[172] Pouria A Mistani, Samira Pakravan, Rajesh Ilango, and Frederic Gibou. Jax-dips: neural bootstrapping of finite discretization methods and application to elliptic problems with discontinuities. Journal of Computational Physics, 493:112480, 2023.

[173] David Johnson, Trevor Maxfield, Yufei Jin, and Ronald Fedkiw. Software-based automatic differentiation is flawed. arXiv preprint arXiv:2305.03863, May 2023. https://arxiv.org/abs/2305.03863.

[174] David Johnson and Ronald Fedkiw. Addressing discontinuous root-finding for subsequent differentiability in machine learning, inverse problems, and control. Journal of Computational Physics, 497:112624, 2024.

[175] David Hyde, Minghao Bao, and Ronald Fedkiw. On obtaining sparse semantic solutions for inverse problems, control, and neural network training. Journal of Computational Physics, 443:110498, 2021.

Appendix A. ENO-WENO Schemes

We provide details on the ENO/WENO schemes used in this work

Appendix A.1. ENO Schemes

In the numerical solution of Hamilton–Jacobi equations and conservation laws, one of the key challenges is to design reconstructions that remain accurate in smooth regions while avoiding spurious oscillations near discontinuities. The Essentially Non-Oscillatory (ENO) schemes address this challenge and are built upon two guiding principles:

1. The upwind direction must be correctly identified,
2. When extending the stencil to construct higher-order interpolants, the additional point should be chosen from the region where the solution exhibits the greatest smoothness, thereby suppressing oscillations near discontinuities.

A convenient framework for constructing polynomial interpolants in the context of ENO reconstructions is provided by Newton's form together with divided difference tables. Consider, for example, a stencil consisting of the grid points x_0, x_1, x_2, and x_3. The Newton representation of the interpolating polynomial is given by:

$$\tilde{u}(x) = \underbrace{a_0}_{\tilde{u}_0(x)} + \underbrace{a_1(x-x_0)}_{\tilde{u}_1(x)} + \underbrace{a_2(x-x_0)(x-x_1)}_{\tilde{u}_2(x)} + \underbrace{a_3(x-x_0)(x-x_1)(x-x_2)}_{\tilde{u}_3(x)},$$

where the coefficients $a_i \in \mathbb{R}$ are found by imposing that:

$$\tilde{u}(x_0) = u(x_0), \quad \tilde{u}(x_1) = u(x_1), \quad \tilde{u}(x_2) = u(x_2), \quad \tilde{u}(x_3) = u(x_3).$$

With this polynomial, the derivative at x_i is expressed as:

$$\frac{d\tilde{u}}{dx}(x_i) = \tilde{u_1}(x_i) + \tilde{u_2}(x_i) + \tilde{u_3}(x_i).$$

The divided-difference table provides a convenient framework for defining the coefficients a_i iteratively. Since $\tilde{u}(x_0) = u(x_0)$, the first coefficient depends only on the initial data point[2], which we denote by

$$a_0 = u[x_0].$$

Once a_0 is known, the next coefficient a_1 is determined from the condition $\tilde{u}(x_1) = u(x_1)$, so that it depends on $u(x_0)$ and $u(x_1)$; we write

$$a_1 = u[x_0, x_1].$$

Proceeding in the same way, we obtain

$$a_2 = u[x_0, x_1, x_2], \qquad a_3 = u[x_0, x_1, x_2, x_3].$$

In general, the divided differences $u[\cdot]$ are defined recursively as

$$u[x_0, \ldots, x_i] \;=\; \frac{u[x_1, \ldots, x_i] - u[x_0, \ldots, x_{i-1}]}{x_i - x_0}.$$

The standard notations are $D^i u = u[x_0, \ldots, x_i]$

The divided differences are particularly useful because their magnitudes provide a measure of the local smoothness of the solution. Specifically, $|D^1 u|$ reflects the strength of the first derivative, $|D^2 u|$ that of the second derivative, and so forth. Consequently, they offer valuable guidance in selecting the most appropriate grid point to add to a stencil.

Third-Order ENO Reconstruction:

In this work we employ the third-order ENO (ENO3) scheme. Suppose that the characteristic direction is determined by λ. The construction of the interpolant proceeds as follows:

[2] Indeed, $a_0 = u(x_0)$.

Step 1. Upwind selection.. The first-order interpolant $\tilde{u}_1(x)$ must account for the upwind direction:

$$\tilde{u}_1(x) = \begin{cases} D^1_{i-\frac{1}{2}}, & \lambda \geq 0, \\ D^1_{i+\frac{1}{2}}, & \lambda < 0. \end{cases}$$

Step 2. Second-order extension.. To avoid including discontinuities, the stencil is extended by comparing smoothness indicators. For instance, if $\lambda < 0$ the first step involves the points (x_i, x_{i+1}). The candidates for extension are x_{i-1}, associated with D^2_i, and x_{i+2}, associated with D^2_{i+1}. The second-order term is chosen as

$$\tilde{u}_2(x) = \begin{cases} D^2_i, & |D^2_i| \leq |D^2_{i+1}|, \\ D^2_{i+1}, & \text{otherwise.} \end{cases}$$

Step 3. Third-order extension.. The procedure is repeated at the third level. Suppose D^2_i was selected at Step 2. The candidates are then x_{i-2} (associated with $D^3_{i-\frac{1}{2}}$) and x_{i+2} (associated with $D^3_{i+\frac{1}{2}}$). The third-order contribution is

$$\tilde{u}_3(x) = \begin{cases} D^3_{i-\frac{1}{2}}, & |D^3_{i-\frac{1}{2}}| \leq |D^3_{i+\frac{1}{2}}|, \\ D^3_{i+\frac{1}{2}}, & \text{otherwise.} \end{cases}$$

Interpolant and derivative.. In this example, assuming $|D^3_{i-\frac{1}{2}}| \leq |D^3_{i+\frac{1}{2}}|$, the reconstructed polynomial is

$$\tilde{u}(x) \;=\; D^0_i + D^1_{i+\frac{1}{2}}(x - x_i) + D^2_i(x - x_i)(x - x_{i+1}) + D^3_{i-\frac{1}{2}}(x - x_i)(x - x_{i+1})(x - x_{i-1}).$$

From this expression, the derivative at x_i follows directly:

$$\begin{aligned} \tilde{u}_x(x) \;=\; & D^1_{i+\frac{1}{2}} + D^2_i\,[\,2x - (x_i + x_{i+1})\,] \\ & + D^3_{i-\frac{1}{2}}\Big(3x^2 - 2x(x_i + x_{i-1} + x_{i+1}) + (x_{i-1}x_i + x_i x_{i+1} + x_{i-1}x_{i+1})\Big). \end{aligned}$$

Notation: In the case $\lambda > 0$, the upwind stencil involves the points i and $i-1$. We denote by $D^-_x u$ the corresponding approximation of $u_x(x_i)$. Conversely, when $\lambda < 0$, the upwind stencil involves the points i and $i+1$, and we denote by $D^+_x u$ the approximation of $u_x(x_i)$.

Appendix A.2. WENO Schemes

As described in Appendix A.1, the ENO scheme selects among three candidate stencils, first by enforcing the correct upwind direction and then by avoiding stencils that cross discontinuities. In smooth regions, a weighted convex combination of these stencils yields higher-order accuracy. This principle forms the foundation of the Weighted Essentially Non-Oscillatory (WENO) schemes.

We illustrate the construction for the approximation of $D^-_x u$; the case of $D^+_x u$ follows analogously. The three possible ENO approximations of $D^-_x u$ are given by

$$\begin{aligned} u^1_x &= \tfrac{1}{3}d_1 - \tfrac{7}{6}d_2 + \tfrac{11}{6}d_3, \\ u^2_x &= -\tfrac{1}{6}d_2 + \tfrac{5}{6}d_3 + \tfrac{1}{3}d_4, \\ u^3_x &= \tfrac{1}{3}d_3 + \tfrac{5}{6}d_4 - \tfrac{1}{6}d_5, \end{aligned}$$

where the finite differences are defined as

$$d_1 = \frac{u_{i-2} - u_{i-3}}{\Delta x}, \quad d_2 = \frac{u_{i-1} - u_{i-2}}{\Delta x}, \quad d_3 = \frac{u_i - u_{i-1}}{\Delta x}, \quad d_4 = \frac{u_{i+1} - u_i}{\Delta x}, \quad d_5 = \frac{u_{i+2} - u_{i+1}}{\Delta x}.$$

The WENO approximation of $D^-_x u$ is constructed as a convex combination of the above stencils:

$$D^-_x u \;=\; \omega_1 u^1_x + \omega_2 u^2_x + \omega_3 u^3_x, \tag{A.1}$$

where the nonlinear weights ω_k are chosen such that the scheme achieves fifth-order accuracy in smooth regions while retaining the ENO property near discontinuities. By construction, the weights satisfy $\omega_1 + \omega_2 + \omega_3 = 1$. The optimal (linear) weights that give fifth-order accuracy in smooth regions are $\{0.1, 0.6, 0.3\}$.

The nonlinear weights are obtained through the following procedure:

- **Smoothness indicators.** For each stencil, define

$$\begin{aligned} S_1 &= \tfrac{13}{12}(d_1 - 2d_2 + d_3)^2 + \tfrac{1}{4}(d_1 - 4d_2 + 3d_3)^2, \\ S_2 &= \tfrac{13}{12}(d_2 - 2d_3 + d_4)^2 + \tfrac{1}{4}(d_2 - d_4)^2, \\ S_3 &= \tfrac{13}{12}(d_3 - 2d_4 + d_5)^2 + \tfrac{1}{4}(3d_3 - 4d_4 + d_5)^2. \end{aligned}$$

- **Nonlinear coefficients.** Define

$$\begin{aligned} \alpha_1 &= \frac{0.1}{(S_1 + \epsilon)^2}, \\ \alpha_2 &= \frac{0.6}{(S_2 + \epsilon)^2}, \\ \alpha_3 &= \frac{0.3}{(S_3 + \epsilon)^2}, \end{aligned}$$

  with $\epsilon = 10^{-6} \max(d_1^2, d_2^2, d_3^2, d_4^2, d_5^2) + 10^{-99}$ to prevent division by zero.

- **Nonlinear weights.** Finally, set

$$\begin{aligned} \omega_1 &= \frac{\alpha_1}{\alpha_1 + \alpha_2 + \alpha_3}, \\ \omega_2 &= \frac{\alpha_2}{\alpha_1 + \alpha_2 + \alpha_3}, \\ \omega_3 &= \frac{\alpha_3}{\alpha_1 + \alpha_2 + \alpha_3}. \end{aligned}$$

The construction of $D_x^+ u$ follows in the same manner, but with the definitions of the finite differences shifted as

$$d_1 = \frac{u_{i+3} - u_{i+2}}{\Delta x}, \quad d_2 = \frac{u_{i+2} - u_{i+1}}{\Delta x}, \quad d_3 = \frac{u_{i+1} - u_i}{\Delta x}, \quad d_4 = \frac{u_i - u_{i-1}}{\Delta x}, \quad d_5 = \frac{u_{i-1} - u_{i-2}}{\Delta x}.$$

We refer the interested reader to [43, 41, 44] for additional details on ENO/WENO schemes.